Charles University in Prague
Faculty of Mathematics and Physics

BACHELOR THESIS

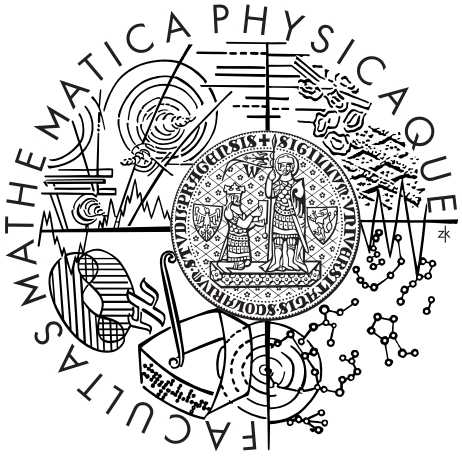

Marek Pšenka

Electrical impedance tomography of soft tissue

Matematický ústav UK

Supervisor of the bachelor thesis: Mgr. Vít Průša, Ph.D.

Study programme: Fyzika

Specialization: Obecná fyzika

Prague 2015

Dedicated to my parents Radim and Dana. Their support made all my endeavours possible. I would also like to thank dr. Průša for his invaluable advice and careful supervision. I am grateful to RS Dynamics for supporting my research and for bringing my attention to this exciting topic.

I declare that I carried out this bachelor thesis independently, and only with the cited sources, literature and other professional sources.

I understand that my work relates to the rights and obligations under the Act No. 121/2000 Coll., the Copyright Act, as amended, in particular the fact that the Charles University in Prague has the right to conclude a license agreement on the use of this work as a school work pursuant to Section 60 paragraph 1 of the Copyright Act.

In ..... date ..... signature of the author

Název práce: Elektroimpedanční tomografie měkkých tkání

Autor: Marek Pšenka

Katedra: Matematický ústav UK

Vedoucí bakalářské práce: Mgr. Vít Průša, Ph.D., Matematický ústav UK

Abstrakt: Bakalářská práce podává přehled o problematice použití elektroimpedanční tomografie (EIT) jako zobrazovací metody se zvláštním důrazem na aplikace ve zdravotnictví. V rámci těchto aplikací je pozornost věnována hlavně snaze detekovat rakovinu prsu pomocí EIT. Autor popisuje motivaci a opodstatnění použití elektroimpedančních technik pro tento účel a shromáždil informace o dosud zkonstruovaných systémech a řešeních této úlohy. Rekonstrukce rozložení vodivosti uvnitř objektů je komplexní problém, který vyžaduje řešení několika podproblémů - výpočtem rozložení potenciálu uvnitř tělesa počínaje a řešením inverzní úlohy konče. Práce popisuje aspekty těchto dílčích problémů a způsob jakým je uchopit matematicky. V závěru je testován softwarový balíček EIDORS, který představuje referenční implementaci algoritmů pro řešení problematiky EIT.

Klíčová slova: elektroimpedanční tomografie, odhad parametrů, inverzní úloha

Title: Electrical impedance tomography of soft tissue

Author: Marek Pšenka

Department: Mathematical Institute of Charles University

Supervisor: Mgr. Vít Průša Ph.D., Mathematical Institute of Charles University

Abstract: This bachelor thesis presents an overview of electrical impedance tomography (EIT) as a proposed imaging technique with special focus on its applications in medicine. Amongst all of the areas being considered, the possibility of performing breast cancer examinations is given special focus. The author dicusses the motivation and rationale behind using EIT for this particular purpose and has gathered information about EIT systems which have been constructed to date. The reconstruction of a conductivity distribution within a physical body is a complex problem which necessitates the solution of a number of subproblems - starting with the calculation of these potential distribution within the body ending with the solution of an inverse boundary value problem. The thesis describes some aspects of these subproblems and presents their mathematical treatment. It concludes by testing the EIDORS software package which represents a reference implementation of algorithms for the EIT problem.

Keywords: electrical impedance tomography, parameter estimation, inverse problem

Contents

1. Introduction

The purpose of this chapter is to discuss the motivation and challenges behind Electrical impedance tomography (EIT) and to summarize its history and current applications, amongst which medical EIT is of main interest. Regarding applications in medicine, the rationale for applying EIT to a particular problem will be discussed and basic aspects of the interaction of electric fields with biological tissues will be studied. To examine the main differences between EIT and well-established imaging techniques, the mechanisms of their operation will be outlined.

Furthermore, special focus will be given to the possibility of performing female breast examinations with EIT. Firstly, arguments, justifying the use of impedance techniques for breast cancer detection will be given. Secondly, a number of breast EIT systems, which have been constructed to date will be reviewed to outline the approaches to breast scanning by impedance tomography.

1.1 What is the motivation of EIT?

Electrical impedance tomography (EIT) is an imaging technique which attempts to provide information about the interior electrical properties of a body under consideration. Its main objective is to reconstruct the distribution of electrical conductivity inside the body by acquiring a set of voltage measurements from electrodes positioned on its boundary - *the inverse problem*. Optionally, determining both the amplitude and phase angle of the voltage measurements can provide information about both conductivity and permittivity, allowing for the reconstruction of the admittivity distribution within the object.

The goal of EIT development is to provide a cost-effective imaging modality mainly for geophysical, industrial and medical applications. This thesis will focus on some of the means of using EIT to monitor the physiology of organ systems and to detect malignant tissue. Unlike many established imaging modalities in medicine such as Computed Tomography (CT), Positron Emission Tomography (PET) and Mammography, EIT does not expose the patient's body to ionizing radiation and the electrical current applied during the scanning process conforms to limitations on its magnitude as well as on the total amount of power dispersed within the subject as prescribed by safety standards.

However, the advantages of using electricity to scan the human body have to be traded off against the quality of the images produced. Poor spatial resolution compared to that of established imaging techniques is seen as a major disadvantage. It can be attributed to the complexity of the inverse problem which is highly nonlinear compared to that of i.e. Computed Tomography.

The topic of medical EIT, including the justification of use, will be further discussed later in this chapter.

1.2 What are the challenges of EIT?

The design of an acquisition circuit collecting boundary measurements must be suited for a given application of EIT. For example, fast acquisition of voltage measurements is necessary in medical applications for patient comfort and in situations, where the time-difference character of a succession of images offers valuable information. Naturally, designing such a circuit while avoiding parasitic effects has its difficulties.

Based on the description given in section 1.1, from a mathematical point of view, EIT can be classified as an inverse boundary value problem. In a situation, where we measure a response (output) of a system to a particular stimulus (input) to study the system structure, we are dealing with an inverse problem. In theory, a set of all possible boundary measurements does uniquely determine the admittivity distribution in the interior of the body of interest [121]. This complete set of measurements is highly ideal, as in practice, only a reduced set may be obtained. The challenge here is to optimize the placement of electrodes and make a suitable choice of stimulation and measurement patterns for a given placement.

Furthermore, specifically adapted inversion techniques must be employed to tackle this problem, since when attempting the reconstruction of images through numerical calculations the resulting system of equations is *ill-conditioned*. Meaning that, without the help of *regularization* techniques designed to treat this 'deficiency', it would not be possible to obtain any results. These advanced methods are usually based on imposing constraints on the sought solution based on available a priori information such as an estimate on the conductivity distribution or its smoothness.

In addition to these difficulties, the solution to the inverse problem necessitates the ability to determine electric fields in the interior of the body for each stimulation pattern given its geometry and a chosen electrode placement - *the forward problem*. For certain special geometries, these may be determined analytically. For arbitrary shapes of the body of interest, the finite element method (FEM) is well-suited. Furthermore, the formulation of the problem in finite elements has to include a description of electrode placement, while accounting for physical effects occurring at the electrode-skin contact.

In summary, the design of an integrated EIT system requires a consideration of all problems mentioned above and prompts collaboration between mathematicians, physicists, engineers and professionals working in the desired area of application.

1.3 History

The idea of using electric fields and related natural phenomena to inspect a physical object via measurements obtained on its boundary has been first put into practice in geophysics. Determining soil resistivity using an arrangement of electrodes placed on the earth's surface was described around the year 1920 by the Schlumberger brothers. These techniques were further improved to allow for 1D lateral and vertical profiling of the resistivity of Earth's surface, laying the foundations of 2D profile reconstruction. The ideas were expanded to the

third dimension by Electrical Resistivity Tomography (ERT), an analogue of EIT where one is only concerned about the real part of the admittivity. The omission of capacitive effects is acceptable in geophysics, since the resistivity carries the majority of information about the composition of soil. An overview of the techniques employed in geophysical resistivity surveys can be found in [88] [75].

Moreover, many important developments in the early theory of inverse problems can be traced back to geophysics. An important figure in the field of inverse problem theory and regularization was Andrey Nikolayevich Tikhonov, a prominent Russian mathematical physicist, who lived in the 20^{th} century. Geophysics was one of Tikhonov's main areas of interest and during the World War 2, he was tasked by the Geophysical Institute of the USSR Academy of Sciences to investigate the effectiveness of DC electrical prospecting methods [138]. Tikhonov was well aware of the ill-posedness of the inverse problem and such problems were still considered impossible to solve at the time. He was surprised when his collaboration with practical geophysicists yielded useful results which led to the discovery of oil deposits in the Ural region. The geophysicists were able to solve the inverse problem by restricting their search to solutions which were intuitively more likely and natural. This led Tikhonov to incorporate a mathematical analogue of intuition into the solution to inverse problems, and in 1943 the foundation to Tikhonov regularization theory for solving ill-posed inverse problems was laid [125].

Amongst the first research works taking on the challenge of focusing the techniques described so far on medical applications are [59], [68], [13]. Researchers of Sheffield University D. C. Barber and B. H. Brown [14] are credited with the first tomographic image produced by EIT - a cross-section of a human forearm.

1.4 The EIDORS software package

In this section a result of a joint effort of a number of EIT researchers to provide a unified software base for EIT image reconstruction. Utility of the EIDORS suite will be further studied in this thesis. A description of some of the forward and inverse techniques it employs will be given along with examples of use. The system offers a variety of possible treatments of both forward and inverse problems compiled from various researchers and represents an important vantage point overlooking the current state of EIT image reconstruction research.

Around the year 2000, EIT research consisted of the efforts of separate teams, each taking a slightly different approach to the problem. Hand in hand came differences in implementation and consequential mutual incompatibility of software solutions to the forward and inverse problems of EIT and other related imaging methods like Electrical Capacitance Tomography (ECT) and Diffuse Optical Tomography (DOT).

An attempt to provide a unified software base for EIT and similar problems was made by the cooperation of researchers at the University of Kuopio Finland and the University of Manchester Institute of Science and Technology (UMIST) (now a part of the University of Manchester) starting the Electrical Impedance and Diffuse Optical Reconstruction Software (EIDORS) project [85]. The 2D EIDORS software package based on Matlab code developed earlier at Kuopio [128]

was released under the GNU General Public License and offered the possibility of using finite element meshes generated by external software. The forward solver used the complete electrode model and supported linear or quadratic elements, while reconstruction was based on the regularized Newton's method, using a discrete differential operator to impose a priori smoothness on the solution.

However, the developers soon saw the need for a full 3D approach as no good approximation to the 3D problem using 2D reconstruction was ever found. Code, enabling the three-dimensional approach, was written at Kuopio [130], but could not have been released due to commercial license limitations. In 2002, researchers at UMIST released the 'EIDORS 3D' software package [108] offering some of the features of the Kuopio code, based on the doctoral thesis of Polydorides [107]. The Matlab system provided model interface between forward and inverse solvers for the full 3D problem along with basic image visualization capabilities. Its implementation allows for handling of arbitrary finite element meshes generated by external software and offers built-in support for the Netgen mesher in particular [113]. Integration with Netgen allows for an accurate introduction of the electrodes and their positions into the model, namely control over mesh refinement near contact surfaces according to their shape.

The years following the release of EIDORS3D saw a tendency of researchers to download the software and customize it to suit their needs. Resulting modifications of EIDORS code were usually mutually incompatible and did not fit the idea of a common software base for all purposes. This lack of extensibility and modularity was remedied by complete restructuralization of the EIDORS3D codebase [9] offering object-oriented approach to the data structures handled, interface for plug-ins and caching capabilities. The package is currently hosted at Sourceforge and may be used freely under the GNU General Public License. A brief overview of the new system architecture and examples of use (including common pitfalls) is given by Adler & Lionheart in [10].

2. Can EIT be of help in medicine?

In this chapter, an overview of the response of biological tissues to applied electrical fields will be given. Physical quantities, used to measure these characteristics (termed 'dielectrical properties'), will be introduced, and a brief review of reported values of these quantities will be assembled and presented in both tabular and graphical format. Furthermore, potential areas of applicability of EIT in medicine will be listed, amongst which screening for breast cancer is of main interest to this thesis. To lay a reliable foundation to the claims to be made, rationale for the use of electroimpedance techniques for breast scanning will be discussed.

2.1 Dielectrical properties of tissues

2.1.1 General properties and approximate models

Tissues of living organisms are complex structures consisting of an arrangement of cells interleaved with extracellular space. Individual cells are surrounded by semipermeable membranes composed of lipids that give the cells capacitive properties. Extracellular and intracellular space both contain water with varying amounts of ions dissolved in it which conducts electricity fairly well [139], [61, p. 411]. Thus when an alternating electric field with angular frequency ω is applied, we describe the electrical properties of tissue using electrical admittivity (the reciprocal of impedivity) to account for both conductivity and specific reactance

$$\gamma(x) = \sigma(x) + i\omega\varepsilon_0\varepsilon_r(x)$$

where $\sigma(x)$ is electrical conductivity measured in Siemens per meter ($\mathrm{S{\cdot}m^{-1}}$), i is the imaginary unit, ε_0 is the dielectric constant of free space, $\varepsilon_r(x)$ is the relative permitivity. The dielectric constant of free space and the relative permittivity may be combined $\varepsilon_0\varepsilon_r(x) = \varepsilon(x)$ to form a quantity called the permittivity, the unit of which is Farad per meter ($\mathrm{F{\cdot}m^{-1}}$). Here both conductivity and permitivity vary with spatial position and need to be represented by a function of the position vector $x \in \mathbb{R}^3$, characterizing their distribution within the body of interest. The entire imaginary part of the admittivity is called the susceptivity and characterizes the specific reactance of the material.

In order to avoid confusion, it has to be noted, that some authors introduce complex relative permittivity in the form

$$\varepsilon_r^*(x) = \varepsilon_r'(x) + i \cdot \varepsilon_r''(x)$$

Where the real part represents the relative permittivity $\varepsilon_r'(x) = \varepsilon_r(x)$ and the imaginary part satisfies $\varepsilon_r''(x) = \sigma(x)/\omega\varepsilon_0$. Furthermore, the term 'dielectric constant' is sometimes used to represent the relative permittivity. However, the use of this term is deprecated and should be avoided.

To describe the dependence of the admittivity of biological tissue on frequency we briefly consider the equivalent impedivity (the reciprocal of admittivity) representation. To characterize a cell as an impedance, we may take a model circuit

consisting of a parallel connection of a resistor (R_e) representing the resistance of the extracellular space with a serial connection of a capacitor (C_m) representing the capacitive effects of the cellular membrane and a resistor (R_i) modeling the intracellular resistance [61, p.411].

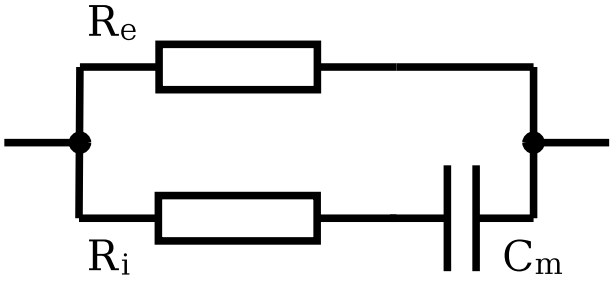

Figure 2.1: Simple equivalent circuit of a cell

At low frequencies, current cannot enter the intercellular environment because of capacitive effects at the membrane, and is therefore restricted to the extracellular space, which represents a minority in the composition of tissue in general, and thus the resulting overall impedance is mostly real and relatively high. As the frequency of the current applied increases, the reactance of the membrane decreases, permitting current flow through the parallel connection of R_e and R_i. The impedance at frequencies sufficient for the omission of membrane reactance is again mainly real and smaller than at low frequencies. As this system is taken between the two "extremal" points by increasing the frequency of the applied current a particular value ω_c called the center frequency is passed which is a useful characteristic of an impedance since at this frequency, the amount of current conducted by the intracellular space is maximum.

Furthermore, when the dependence of permittivity on the frequency of the applied current of many types of biological tissue is plotted, the resulting curve is decreasing (reactance decreases) with three characteristic steps called the α-dispersion, β-dispersion and γ-dispersion regions [117]. The α-dispersion region is usually centered at 100 Hz. β-dispersion occurs in the 10 kHz - 10 MHz range with γ-dispersion being found at higher frequencies. The biophysical mechanisms responsible for these phenomena are outside the scope of this thesis. However, they are of interest to EIT practice focused on detecting malignant tissue, since the majority of changes between normal and pathological tissue has been found to occur in the α and β regions [17]. Therefore EIT systems typically operate between 100 Hz and 100 MHz [61, p. 411]

2.1.2 Review of tabulated data

An important study of the dielectric properties of various types of tissue from different samples across mammalian species is given by Gabriel et. al [47], [48], [49]. In [47] a review of dielectric characteristics from numerous sources over the second half of the 20^{th} century is given in convenient graphical format. The authors provide their own experimental data in [48] and compare them to the previously reported measurements. To complete their investigation, parametric models for the description of the dependence of electrical properties of tissue on

frequency are introduced in [49]. In addition to these important research works, Gabriel C. gives a compilation of the dielectric properties of tissue at RF and microwave frequencies in [46]. This technical report presents data quantifying the variation of dielectrical properties of different types of tissue extracted from multiple species with frequency in both graphical and tabulated format.

To help form a qualitative picture of the response of tissue to electric fields a brief summary of the dielectrical properties of select tissues was assembled and will be presented in both tabular and graphical format.

Table 2.1 contains the values of relative permitivity ε_r and conductivity σ for blood, fat, lung tissue, muscle tissue and skin in the range of frequencies commonly used by EIT as reported in [46]. All measurements were carried out at 37 °C with the data set species specification given in parentheses. Skin measurements were carried out on a human forearm in-vivo. Values presented by the table are plotted in figure 2.2.

Even though tissue samples were extracted from various mammals, the data shown should not be considered misleading. While there are certainly morphological differences between tissues of individual mammalian species, the data compiled by [47] providing a species-wise comparison, suggest the variations for a given frequency and tissue type may well fall within the uncertainties of the presented measurements and are not of systematic origin [46, p. 7]. Surely, there is an amount of uncertainty associated with the measurement of dielectric properties of tissue, that can never be eliminated solely because it is, amongst other factors, influenced by the heterogeneity of samples acquired from one species. This stems from the fact, that dielectrical properties of tissue depend upon the chemical content, temperature, time elapsed since the sample was extracted (in vitro, as opposed to in vivo).

To support this argument, let us examine the first two data sets of table 2.1 outline the dependence of dielectrical properties of fatty tissue on frequency. By comparing the two data sets representing human breast fat tissue and bovine fatty tissue respectively, it can be concluded that they do not differ significantly. This, although inconclusively, supports the claim, that the species-to-species difference in dielectrical characteristics is within the uncertainty of measurements.

To confront data in table 2.1 with those provided by other authors, table 2.2 was assembled. It contains data from various samples at different temperatures. The reader is referred to the corresponding sources for details. Data presented by [115] represent a compilation of results from multiple researchers sampling tissues of different mammals at various temperatures. The measurements in [116],[105] were taken at 37 °C. When a value in the form of a/b for lung tissue is given, a represents the value in inflated state, whereas b represents the value in deflated state.

Figure 2.2: Conductivity and permittivity data from table 2.1 plotted against frequency. Notable difference between the dispersion behavior of different types of tissue is apparent. On the other hand, values of both conductivity and permittivity for bovine fatty tissue and human breast fat are in agreement, supporting the claim that species-wise variations in the dielectrical properties of the same type of tissue are not of systematic origin

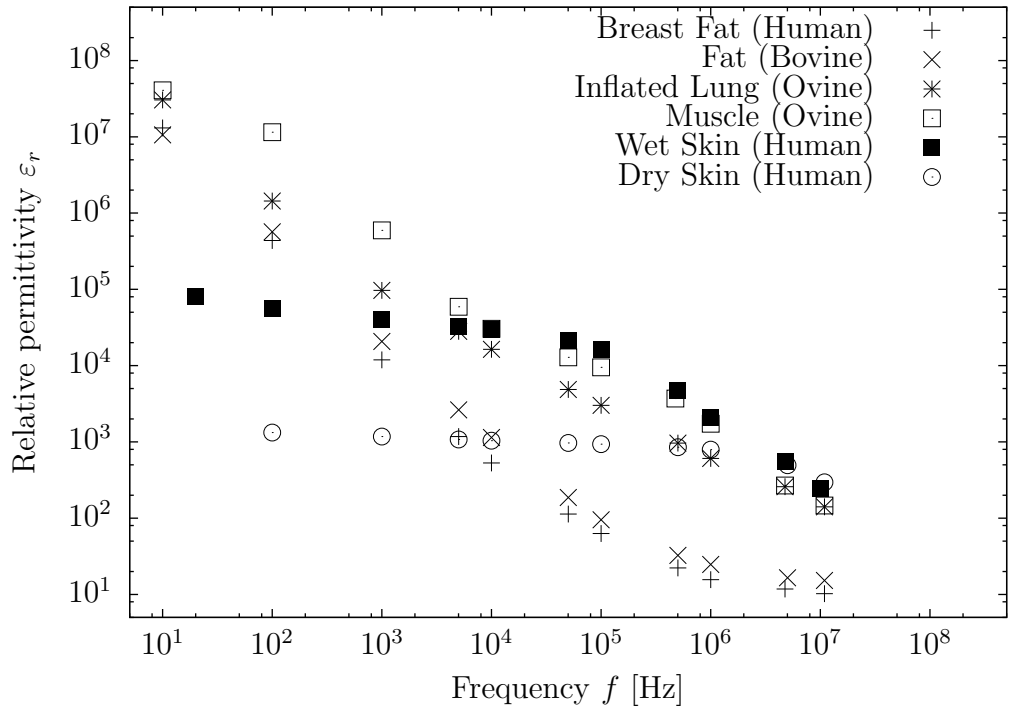

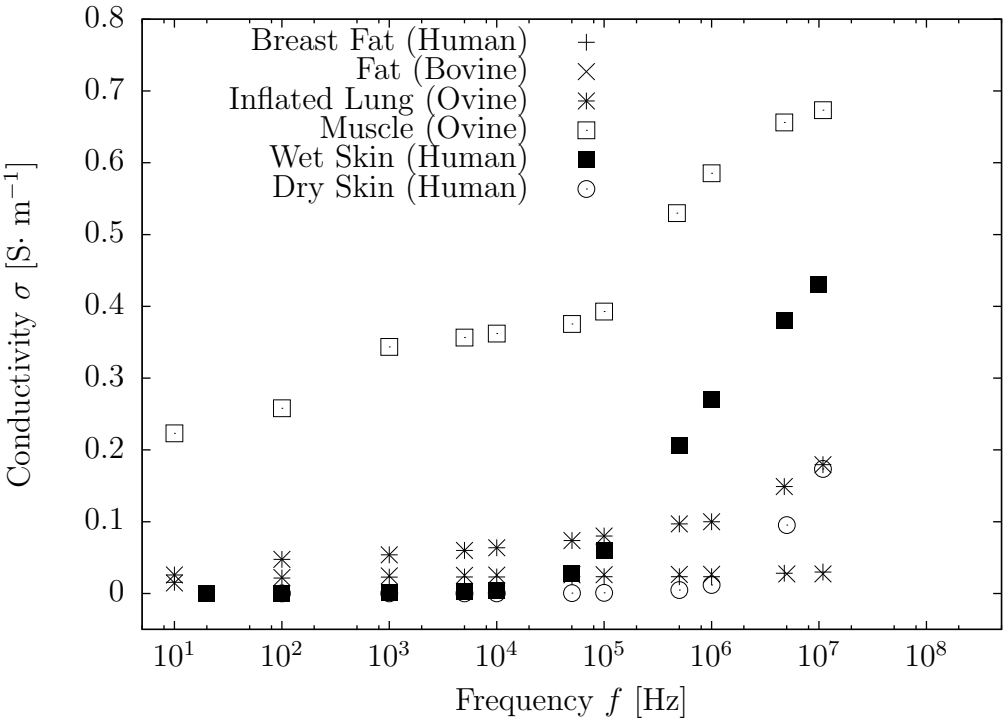

Table 2.1: Dielectrical properties of tissues as presented by [46]

Breast Fat (Human)			Fat (Bovine)		
f [Hz]	ε_r	σ [S·m^{-1}]	f [Hz]	ε_r	σ [S·m^{-1}]
10	$1.3 \cdot 10^7$	$1.57 \cdot 10^{-2}$	10	$1.1 \cdot 10^7$	$1.46 \cdot 10^{-2}$
100	$4.3 \cdot 10^5$	$2.15 \cdot 10^{-2}$	100	$5.7 \cdot 10^5$	$2.23 \cdot 10^{-2}$
$1 \cdot 10^3$	$1.2 \cdot 10^4$	$2.29 \cdot 10^{-2}$	$1 \cdot 10^3$	$2.1 \cdot 10^4$	$2.46 \cdot 10^{-2}$
$5 \cdot 10^3$	$1.2 \cdot 10^3$	$2.31 \cdot 10^{-2}$	$5 \cdot 10^3$	$2.6 \cdot 10^3$	$2.53 \cdot 10^{-2}$
$1 \cdot 10^4$	$5.3 \cdot 10^2$	$2.31 \cdot 10^{-2}$	$1 \cdot 10^4$	$1.1 \cdot 10^3$	$2.56 \cdot 10^{-2}$
$5 \cdot 10^4$	$1.1 \cdot 10^2$	$2.35 \cdot 10^{-2}$	$5 \cdot 10^4$	$1.9 \cdot 10^2$	$2.60 \cdot 10^{-2}$
$1 \cdot 10^5$	$6.2 \cdot 10^1$	$2.35 \cdot 10^{-2}$	$1 \cdot 10^5$	$9.5 \cdot 10^1$	$2.62 \cdot 10^{-2}$
$5 \cdot 10^5$	$2.2 \cdot 10^1$	$2.34 \cdot 10^{-2}$	$5 \cdot 10^5$	$3.3 \cdot 10^1$	$2.65 \cdot 10^{-2}$
$1 \cdot 10^6$	$1.5 \cdot 10^1$	$2.34 \cdot 10^{-2}$	$1 \cdot 10^6$	$2.3 \cdot 10^1$	$2.67 \cdot 10^{-2}$
$4.8 \cdot 10^6$	$1.2 \cdot 10^1$	$2.81 \cdot 10^{-2}$	$5 \cdot 10^6$	$1.7 \cdot 10^1$	$2.74 \cdot 10^{-2}$
$1 \cdot 10^7$	$1.0 \cdot 10^1$	$2.96 \cdot 10^{-2}$	$1 \cdot 10^7$	$1.5 \cdot 10^1$	$2.73 \cdot 10^{-2}$
Inflated Lung (Ovine)			Muscle (Ovine)		
f [Hz]	ε_r	σ [S·m^{-1}]	f [Hz]	ε_r	σ [S·m^{-1}]
10	$3.0 \cdot 10^7$	$2.57 \cdot 10^{-2}$	10	$4.1 \cdot 10^7$	$2.23 \cdot 10^{-1}$
100	$1.4 \cdot 10^6$	$4.76 \cdot 10^{-2}$	100	$1.2 \cdot 10^7$	$2.58 \cdot 10^{-1}$
$1 \cdot 10^3$	$9.7 \cdot 10^4$	$5.39 \cdot 10^{-2}$	$1 \cdot 10^3$	$5.9 \cdot 10^5$	$3.44 \cdot 10^{-1}$
$5 \cdot 10^3$	$2.8 \cdot 10^4$	$6.00 \cdot 10^{-2}$	$5 \cdot 10^3$	$5.9 \cdot 10^4$	$3.57 \cdot 10^{-1}$
$1 \cdot 10^4$	$1.6 \cdot 10^4$	$6.37 \cdot 10^{-2}$	$1 \cdot 10^4$	$3.0 \cdot 10^4$	$3.62 \cdot 10^{-1}$
$5 \cdot 10^4$	$4.9 \cdot 10^3$	$7.38 \cdot 10^{-2}$	$5 \cdot 10^4$	$1.3 \cdot 10^3$	$3.76 \cdot 10^{-1}$
$1 \cdot 10^5$	$3.0 \cdot 10^3$	$8.00 \cdot 10^{-2}$	$1 \cdot 10^5$	$9.5 \cdot 10^3$	$3.93 \cdot 10^{-1}$
$5 \cdot 10^5$	$9.6 \cdot 10^2$	$9.70 \cdot 10^{-2}$	$4.8 \cdot 10^5$	$3.7 \cdot 10^3$	$5.30 \cdot 10^{-1}$
$1 \cdot 10^6$	$5.8 \cdot 10^2$	$1.02 \cdot 10^{-1}$	$1 \cdot 10^6$	$1.7 \cdot 10^3$	$5.85 \cdot 10^{-1}$
$4.8 \cdot 10^6$	$2.6 \cdot 10^2$	$1.49 \cdot 10^{-1}$	$4.8 \cdot 10^6$	$2.7 \cdot 10^2$	$6.56 \cdot 10^{-1}$
$1 \cdot 10^7$	$1.4 \cdot 10^2$	$1.79 \cdot 10^{-1}$	$1 \cdot 10^7$	$1.5 \cdot 10^2$	$6.70 \cdot 10^{-1}$
Wet Skin (Human)			Dry Skin (Human)		
f [Hz]	ε_r	σ [S·m^{-1}]	f [Hz]	ε_r	σ [S·m^{-1}]
20	$8.0 \cdot 10^4$	$2.89 \cdot 10^{-4}$			
100	$5.6 \cdot 10^4$	$3.32 \cdot 10^{-4}$	100	$1.3 \cdot 10^3$	$1.81 \cdot 10^{-4}$
$1 \cdot 10^3$	$4.0 \cdot 10^4$	$7.10 \cdot 10^{-4}$	$1 \cdot 10^3$	$1.2 \cdot 10^3$	$1.80 \cdot 10^{-4}$
$5 \cdot 10^3$	$3.3 \cdot 10^4$	$2.25 \cdot 10^{-3}$	$5 \cdot 10^3$	$1.1 \cdot 10^3$	$2.10 \cdot 10^{-4}$
$1 \cdot 10^4$	$3.0 \cdot 10^4$	$4.49 \cdot 10^{-3}$	$1 \cdot 10^4$	$1.0 \cdot 10^3$	$2.49 \cdot 10^{-4}$
$5 \cdot 10^4$	$2.1 \cdot 10^4$	$2.80 \cdot 10^{-2}$	$5 \cdot 10^4$	$9.7 \cdot 10^2$	$5.34 \cdot 10^{-4}$
$1 \cdot 10^5$	$1.6 \cdot 10^4$	$5.93 \cdot 10^{-2}$	$1 \cdot 10^5$	$9.3 \cdot 10^2$	$8.93 \cdot 10^{-4}$
$5 \cdot 10^5$	$4.7 \cdot 10^3$	$2.06 \cdot 10^{-1}$	$5 \cdot 10^5$	$8.51 \cdot 10^2$	$4.86 \cdot 10^{-3}$
$1 \cdot 10^6$	$2.1 \cdot 10^3$	$2.70 \cdot 10^{-1}$	$1 \cdot 10^6$	$7.9 \cdot 10^2$	$1.19 \cdot 10^{-2}$
$4.8 \cdot 10^6$	$5.5 \cdot 10^2$	$3.80 \cdot 10^{-1}$	$5 \cdot 10^6$	$4.9 \cdot 10^2$	$9.54 \cdot 10^{-2}$
$1 \cdot 10^7$	$2.4 \cdot 10^2$	$4.30 \cdot 10^{-1}$	$1 \cdot 10^7$	$3.0 \cdot 10^2$	$1.74 \cdot 10^{-1}$

Table 2.2: Dielectric properties of select types of tissue. The data was collected from various sources.

	Blood		Fat		Lung		Muscle		Skin	
Frequency f [ref.]	ε_r	σ [S·m^{-1}]	ε_r	σ [S·m^{-1}]	ε_r	σ [S·m^{-1}]	ε_r	σ [S·m^{-1}]	ε_r	σ [S·m^{-1}]
10 Hz [116]						0.088		0.102		
10 Hz [114]						0.063-0.111		0.067-0.125		
100 Hz [114]						0.067-0.125		0.07-0.13		
100 Hz [115]					$450{\cdot}10^3$		$800{\cdot}10^3$			
1 kHz [114]						0.08-0.13		0.08-0.14		
1 kHz [115]	$2.9{\cdot}10^3$	0.56-0.77	$50{\cdot}10^3$	0.04-0.06	$90{\cdot}10^3$	0.1	$130{\cdot}10^3$	0.13		
10 kHz [114]						0.08-0.13		0.08-0.17		
10 kHz [116]			20		25	0.105	55	0.131		
100 kHz [115]	$2.7{\cdot}10^3$	0.68				0.50-0.61	$30{\cdot}10^3$	0.40-0.59		
100 kHz [116]						0.50-0.60		0.42-0.58		
1 MHz [115]		0.71				0.56-0.67	$2{\cdot}10^3$	0.48-0.63		
1 MHz [116]	2040					0.56-0.67		0.50-0.60		
10 MHz [115]	200	1.11				0.67-0.91		0.58-0.67		
13.56 MHz [105]	155	1.16	38	0.21	42/94		112	0.74	120	0.25
27.12 MHz [105]	110	1.19	22	0.21	29/57	0.13/0.32	98	0.76	98	0.4

2.2 Areas of EIT use in medicine

EIT shows potential to be used in a number of areas of clinical practice [61], [15]. It may play an important role in diagnostics, monitoring of diseases and the study of physiological processes as a technique, which is harmless, cheap and fast, would be of great value in those areas. EIT was found to have a plethora of potential application, to name a few, its utility EIT was studied in the following areas: pulmonary function, detection of breast tumors, monitoring of gastric emptying and brain imaging.

To picture the origins of EIT devices, it is important to mention Sheffield APT (Applied Potential Tomography[1]) systems which count among the first EIT devices for potential use in clinical practice constructed [26].

In addition to specific-purpose EIT systems described in the following sections, Multi-purpose devices should be mentioned. A project aimed at generality is the ACT system developed at the Rensselaer Polytechnic Institute [38] the most recent version of which is the ACT-4 (2007) [87]. The ACT-4 was used for breast cancer detection and will be discussed further in section 2.4.

A more recently developed system is the KHU (Kyung Hee University of Korea) apparatus [103], [102] whose present version is the Mark 2.5 (2014) [132] featuring automatic hardware parameter calibration to counteract signal-to-noise ratio decline with long-term usage. Its authors plan to use it in stroke, intracranial bleeding detection, monitoring neural, cardiac activity and ventilation.

The possibility of breast examination using EIT will be discussed in more detail in the next section (2.4.1).

2.2.1 Studying pulmonary function via EIT

The main aspects of pulmonary function studied by EIT are ventilation and detection of blood clots in the lungs. Other imaging modalities such as X-ray imaging, CT and MRI can be used for the same purpose with high spatial resolution. However the patient has to be exposed to ionizing radiation in the process - a drawback EIT seeks to eliminate.

EIT is particularly suited for the imaging of lung ventilation since the conductivity of lung tissue decreases with inhalation of air giving high relative contrast through a succession of images depicting the process of breathing. In terms of instrumentation, a significant number of clinical studies carried out in lung EIT used devices based on the Sheffield systems [26] developed by D.C. Barber and B. Brown who started investigating EIT in the 1980s [13]. These systems use between 8 and 32 electrodes placed in a transverse plane around the thorax. Current is driven through pairs of electrodes and differential voltage measurements are collected. Reconstruction is based on linear, one-step algorithms structurally similar to the original back-projection methods developed in Sheffield.

Recently, a collective of prominent researchers in EIT development centered around the GREIT project [7], focused on consolidating the current state of knowledge regarding lung EIT, assessed the progress made in various clinical applications and gave a summary of their individual technical difficulties and unresolved problems [6]. The authors regarded potential applications in ventilation

[1] an expression for EIT used in the early works of Barber & Brown

imaging as the most promising.

2.2.2 Brain EIT

An attractive possible use of EIT is imaging of the human brain, where it can be used to visualize blood flow, detect ischaemia, stroke and even monitor neuronal activity. One of the main difficulties of brain scanning with EIT is posed by the skull, which is highly insulative. However,there are situations , where an invasive placement of electrodes has its advantages [89]. In the beginning of brain EIT, when only the early Sheffield systems were available, imaging was difficult, since these systems used adjacent drive patterns (driving current through a pair of neighboring electrodes) resulting in very low sensitivity in the center of the head as the majority of the current was shunted by the skull. An another complication in brain EIT reconstruction models is the fact that the skull and white matter are highly anisotropic and thus authors point to the need for incorporation of anisotropy into the formulation of the problem [5].

On a different note, EIT could be used to provide a fast response modality visualizing the brain of stroke patients. In the event of a stroke, it is important to distinguish between the haemorrhagic and ischemic case, because if ischaemic stroke occurs, medication may be administered. This can only be done with the help of scanning as clinical appearances of both types are identical. It has been demonstrated that an attempt to treat ischaemic stroke using thrombolytic agents reduces mortality and the severity of long term consequences. To enable this treatment, the imaging and diagnosis must be carried out rapidly. CT scans are well-suited for imaging of stroke patients, since they have an exquisite sensitivity for the detection of blood. However, it is mostly impossible to obtain an urgent CT scan.

Romsauerova et. al. [110] investigated this possible use of EIT using the UCLH Mk 2 multi-frequency (MFEIT) system [136], [93]. The idea was to use the significant differences in the dependence of conductivity on frequency between ischaemic gray matter and healthy gray matter. However, they were not able to sense this difference using their methods as more accurate measurements over an even broader frequency range are thought to be required. They used a linear reconstruction algorithm employing truncated singular value decomposition (tSVD) while the sensitivity matrix had been derived from an anatomically realistic finite element mesh of the head.

2.2.3 Monitoring the gastrointestinal tract using EIT

Changes in gastric emptying can point to a variety of functional disorders of the gastrointestinal tract. In the past, methods employing ingestion of radioactive dyes by the patient or intubation were used. The benefits of using EIT as a substitute are obvious. EIT has been show to provide a reliable method of gastric monitoring of infants [101], providing a safe means of helping diagnose pyloric stenosis - a narrowing of the opening of the stomach into the first part of the small intestine with relatively high incidence which usually presents symptomatically during the first few weeks after birth [81].

2.3 Comparison of EIT with established imaging techniques

It is without question, that by proponing EIT as an imaging technique in medical practice, researchers stepped into a highly competitive environment. Years before first EIT systems were designed, Computed Tomography (CT) was already a thriving area of research. First CT systems started appearing in the 1970s and their inventors, G. Hounsfield and A. M. Cormack received the Nobel Prize in Physiology or Medicine in 1979. What's more, CT is not the only strong opponent EIT has to prove having an advantage over. In 1971 Paul. C. Lauterbur invented Magnetic Resonance Imaging (MRI) and published the theory supporting the method in 1973 [82]. Lauterbur, along with P. Mansfield, was awarded the 2003 Nobel Prize in Physiology or Medicine for their discovery.

In this section EIT will be compared with these imaging modalities in terms of general advantages, while their performance in breast cancer examination will be discussed in the next section.

2.3.1 Computed Tomography

To obtain an image using a CT system, a source of X-ray radiation is rotated around the body being investigated [60]. A detector facing the source measures the attenuation of the beam after passing through the body with the radial distribution of total beam attenuation along a straight line through the object (a sinogram) constituting the inverse problem data. The attenuation distribution may be viewed as a collection of projections, which are effectively Radon transforms [100] of the object structure. Thus, the spatial attenuation coefficient distribution in a horizontal slice through the object may be recovered by applying an inverse Radon transform, forming the basis of the classical filtered back-projection algorithm for X-ray computerized tomography. The filtered back-projection approach has the advantage of being conceptually simple and computationally undemanding, however, it is susceptible towards certain types of image artifacts and sophisticated reconstruction algorithms came to replace it.

The main advantage of CT compared to EIT is the simplicity of the inverse problem, requiring less mathematical treatment than EIT reconstruction. Namely, CT does not demand the ability to carry out forward computations, its inverse problem is well-posed and does not require conditioning via regularization Furthermore, Computed Tomography may be considered a true tomographic method, since X-rays traveling through the human body practically do not deflect outside the plane to be imaged, while EIT needs to address the necessity of taking a 3D approach to image reconstruction because electric current travels through 'paths of least resistance' and can not be confined to a plane by EIT current driving systems.

However, a CT scanning procedure cannot be carried out without exposing the patient to X-ray radiation, which has gradually come to be a cause for concern amongst medical professionals [24] and poses a risk to the patient's health. This drawback of any X-ray based method provides motivation for the development of alternative imaging techniques based on different physical phenomena such as EIT.

2.3.2 Magnetic Resonance Imaging

Like EIT, Magnetic Resonance Imaging (MRI) is based on the physics of electromagnetic fields, however, its means of operation are based on a different aspect of electromagnetism [27]. To perform an MRI scan on a human subject, the patient's body has to be permeated by a strong magnetic field (0.1 - 3.0 T) which aligns the angular momenta of hydrogen atoms in water molecules representing a major constituent of the tissues of living organisms. The body is then subjected to a Radiofrequency (RF) pulse at a frequency determined by the magnitude of the static magnetic field, causing a change in the direction of the hydrogen magnetic momenta, which will then relax to a stable state in a certain relaxation time by emitting RF pulses. Different types of tissue had been shown to relax at different times and this phenomenon forms the basis of the distinguishability of various types of tissue by MRI. To allow for spatially specific imaging, gradient coils varying the magnetic field linearly throughout the imaged volume are used, causing a variation in the RF frequency of the re-emitted pulse enabling the determination of the position where it originated.

There are a number of ways of improving the clinical utility of EIT. For example, when aiming to sense the contrast between benign and malignant tissue using MRI, gadolinium is administered to highlight the difference between responses of healthy and cancerous tissue. Furthermore, an another variant of the technique which proved useful is functional imaging, where physiological changes in tumor tissue are used to distinguish it from its surroundings. One of such techniques is Diffusion Weighted Imaging (DWI) based on probing the flow of water through cancerous masses in the female breast [79] as it is restricted in tumours due to the increased packing density of the tissue.

As a breast scanning modality, MRI offers high sensitivity without subjecting the patient to ionizing radiation. However, the sophistication of the method is a cause for the high cost per scan and is seen as a significant disadvantage. Hassan & El-Shenawee conducted a large-scale investigation into the characteristics of different imaging techniques for breast cancer detection based on electromagnetism and reviewed their success in clinical environments [58]. Individually, MRI showed the highest sensitivity of all the methods presented.

2.4 EIT and cancer of the breast

Over the period of EIT development, screening for breast cancer has gradually become one of the most active areas of research. It can be argued, that amongst all of the potential applications where utility of EIT is being investigated, breast cancer detection has had the biggest number of positive results. One of the reasons for this, is the fact that the breast can be seen as an extremal part of the human body and thus can be surrounded by electrodes easily, whereas in other medical applications, researchers have to deal with the insulative properties of the skull, ribcage etc. Furthermore, an another great source of success of the method is the significant difference between normal and malign breast tissue implying a level of contrast in the reconstructed distributions which was shown to have diagnostic value. This section provides evidence for the claims made in this paragraph and reviews some breast EIT systems which had been developed over the years of EIT research. For a quick summary of the most important features of these systems, the reader is referred to figure 2.3.

2.4.1 Motivation & rationale

According to the 2014 World Cancer Report by the World Health Organization breast carcinoma is the most common type of invasive cancer in women and accounts for more than 20% of all cases of invasive cancer in women. As a preventive measure, regular screening using mammography, for women deemed at risk was introduced.

However, conclusions reached by P.C. Gotzsche [53] in the 2009 Cochrane report on regular breast examination with mammography suggest that investments into new screening methods for breast cancer detection are reasonable. To draw a bottom line on regular breast cancer screening, the authors state the following

> '..., screening appears to lower breast cancer mortality. However, the chance that a woman will benefit from attending screening is very small, and considerably smaller than the risk that she may experience harm. It is thus not clear whether screening does more good than harm.'.

This is due to the low specifity[2] of the technique, which requires the use of additional diagnostic methods amongst which biopsy of the suspicious tissue is common. The results of biopsies are negative in a great number of cases [28]. Furthermore, low specifity implies a risk of overdiagnosis and overtreatment. In addition to exposing the patient's body to x-rays mammography screenings are known to cause a significant amount of discomfort to patients. In conclusion, even though the benefits of screening generally outweigh the possible harm done by X-ray exposure [43], the fact that it may increase the risk of developing cancer is undeniable.

In summary, there is a clear demand for a low-risk imaging modality having the potential to replace mammography in terms of specifity in female breast examination. A number of medical professionals and EIT researchers believe impedance imaging may fulfill these requirements. Support for this proposition

[2] the ability of an examination to distinguish between harmless and pathological findings

has to be built by discovering consistent means of distinguishing between healthy breast tissue and various malformities.

Attempts to test the hypothesis that the dielectrical properties of malignant and healthy tissue differ, date back to the 1920s [45]. This research helped fuel the investigation into possible methods of medical examination utilizing dieletrical properties.

A suitable startpoint for the investigation into the current state of knowledge regarding the contrast between malignant and normal breast tissue is an article by Y. Zou [139], which reviews the findings of a number of researchers who gathered in vivo and in vitro comparative measurements of the dielectrical characteristics of normal and cancerous breast tissues. From the reviewed in vitro data, its authors draw a clear conclusion, that there are significant differences in electrical impedance between healthy and malignant tissue. To be precise, cancerous tissues were shown to have a higher conductivity and/or permittivity. This is attributed to various morphological differences between healthy and cancerous cells of corresponding type and altered structure of the tissue itself. For example, J. Jossinet reported that the modulus of impedivity of cancerous tissue (about $400\Omega\cdot$ cm at 1 kHz) is lower than that of non-pathologic fatty tissue (about $2000\Omega\cdot$ cm) [69], [67].

Additionally, data from reviewed in vivo measurements further support the claim, that cancerous breast tissues have lower impedance. In addition, results by Morimoto et. al. [96] were reviewed, suggesting impedance techniques may be specific regarding benign vs. malignant contrast. The authors presented results, obtained from in-vivo invasive measurements, in the form of characteristics of the equivalent circuit described earlier in section 2.1. Their results showed that C_m of breast cancer tissue was 'significantly lower than that of benign tumors', while R_e, R_i of malignant breast tumors were 'significantly higher than those of benign lesions'.

Research into the dielectrical properties of breast tissue carried out by J. Jossinet laid the foundation to investigations into the possibility of distinguishing between malignant and normal breast tissue by acquiring impedance measurements over a frequency range. In 1998, he acquired a set of 120 impedivity spectra of breast tissue immediately after excision through the 488 Hz - 1 MHz frequency range [70].

Three groups of tissue were examined - normal tissue, benign pathological tissue and carcinoma tissue. The first important observation Jossinet made is the fact that there is no significant correlation between impedivity and patient age (except in the mastopathy case). An another encouraging discovery was made - according to the author, there is no signifcant difference between groups of normal tissue and those exerting benign pathology. Finally, it was found, that the carcinoma group differed from all other groups by low-frequency-limit resistivity, fractional power and the phase angle at frequencies above 125 kHz. The results of the study indicate that impedance spectroscopy may be applicable as a method of diagnosing breast cancer.

Upon the basis of his previous research, Jossinet proposed methods, based on the statistical analysis of breast tissue impedance spectra, to discriminate between several classes of breast tissue [39]. He tested his ideas on a data set comprising 106 cases with overall classification efficiency of approximately 92%,

while being able to correctly identify carcinomas in 86% of cases. By achieving a sensitivity and specifity rate this high, using an impedance-based technique for breast cancer detection, Jossinet's study undoubtedly provided encouragement to all researchers aiming to utilize electrical impedance methods in breast cancer examination.

2.4.2 Approaches to breast EIT

Approaches to breast EIT may be divided into three main branches - electrical impedance mapping (EIM), tomographic imaging and full 3D reconstruction.

Firstly, it should be noted, that the 'EIM' abbreviation is also used to represent a more general term - Electrical Impedance Mammography. EIM systems usually employ a rigid planar array of electrodes which is pressed against the patients breast. This may be seen as an advantage in itself, as the breast is compressed to form a thin layer between the array and the ribcage. To sink the current brought in by a chosen electrode of the array, a distant electrode is used, usually held in the patient's hand.

An another advantage of EIM devices is the relative simplicity of the solution to the inverse problem employed by these systems. These systems usually perform image reconstruction based on back-projection methods, which do not require the same degree of sophisticated treatment as conceptually more complex methods.

In tomographic imaging systems, the electrodes are placed in a rigid circular array inside a scanning head surrounding a region of the plane defining a 2D slice through the breast which is inserted into the scanning head of the device. It has to be noted, that EIT cannot be considered a true tomographic modality and thus the T in EIT is a bit of a misnomer. This is because electrical current travels through 'paths of least resistance' and can never be confined to a plane as opposed to X-rays used by CT. Scanning heads for tomographic systems may contain more than one array and allow for imaging at different depth levels.

The attempt to account for and capture this 'deflection' of current outside the plane defined by a planar arrangement of electrodes is made by full 3D reconstruction, which utilizes measurements captured by a scanning head with various electrode arrangements to reconstruct 3D conductivity distribution for the domain representing the breast as a whole.

Pilot developments of breast scanning applications of EIT had shed more positive light on the most important question - Can EIT provide a reliable imaging modality which performs comparably or as an adjunct to other methods?

2.4.3 Electrical impedance mapping (EIM) devices

The T-Scan TS2000

In the early days of EIT development Piperno et. al. conducted a large scale clinical study on the effectiveness of various modalities of breast cancer detection [106]. One of the techniques investigated was the 'Mamoscan' EIM device which was further developed and later marketed as the 'TS2000' [11] and approved by the Food and Drug Administration of the United States as an adjunct to mammography. The study was carried out on 6000 patients, 745 of whom had histologically confirmed malignancies. The results were amongst the earliest

encouragements to EIT researchers, as EIT had the greatest number of correct findings of all 'competitors'. Furthermore, in a total of nine cases, EIT was the only modality to alert the examinators to a presence of a malignancy.

Among other groups, who demonstrated the utility of the TS2000, are Martin et. al. [92] and Glickman et. al. [51]. Glickman et. al. even developed a postprocessing algorithm which automatically recognized bright focal spots on and was able to distinguish between cancerous and benign/normal tissue using predictors. The authors reported sensitivity of 84% and specifity of 52% in a test group of around 600 patients.

TCI'S electric mammograph

An EIM device, simmilar to the TS2000 mentioned above was constructed by Cherepenin et. al. [35], and used 256 electrodes arranged in a square array, the size of which was 12 cm. To reconstruct 'grayscale' horizontal slices of conductivity distribution within the breast, a weighted back-projection method was used. Back-projection methods are analytic in nature and provide an expression for the conductivity $\sigma(x)$.

The device was tested clinically on a sample of 21 women with tumours. The authors claim, that 86% of examinations by EIT were fully or partially consistent with diagnoses made by other independent methods. Furthermore, The device was patented by TCI (Technology Commercialization International Inc. of Albaquerque USA) who supported the research.

A year later, the same group remodeled their electrode array to form a circular pattern improving the potential efficiency of electrodes that were previously planted in the corners of the earlier square arrangement. With this improved device, they had not carried out any clinical examinations, but studied the influence of hormonal changes during menstrual cycles on the attributes of images [36].

MEIK

The research of Cherepenin and his colleagues, conducted at the Institute of Radiotechnology and Electronics of the Russian Academy of Science, formed a knowledge basis for electrical impedance mammography, which was later drawn from by Karpov A.Yu, head of the perinatal department of the Clinical Hospital nr. 9 in Yaroslavl, whose work led to the development of the first "MEIK" electrical impedance mammography system patented in 2003 in the Russian Federation and the US [4]. The MEIK apparatus uses 256 electrodes in a planar array and shares its specifics with earlier devices developed by Cherepenin et. al.

In 2003 SIM-technika ltd. set up commercial production of the MEIK device and after obtaining the necessary approval certificates and the system came to be used in Russia, Europe and Asia. The device was further improved and received EC certification in 2006.

Utility of the system in clinical practice was examined during a study by Campbell et. al. [30] which concluded with encouraging results regarding sensitivity and specifity. Prasad et. al. [109] compared the sensitivity of EIT using the MEIK system to ultrasonography and mammography using a group of 88 patients and found the total sensitivity of EIT comparable to that of mammography. In conclusion, the authors supported the possibility of using EIT as an

adjunct to mammography and ultrasonography in breast cancer detection, but recommended further investigation into the specifity of EIT imaging.

2.4.4 Tomographic imaging

Dartmouth University 1^{st} generation EIS system

The first study to test a tomographic imaging method in clinical environment was carried out by Ostermann et. al [104], who performed absolute reconstruction of permittivity and conductivity distributions within slices using measurements collected by an EIT system derived from the first-generation Electrical Impedance Spectroscopy (EIS) system (2000) developed at Dartmouth College [57].

Unlike in the majority of EIT devices, data is acquired in voltage drive mode - voltages are applied and currents are measured. In addition, data is collected at multiple frequencies to obtain information of spectroscopic nature. Image reconstruction was based on the Newton method and the solver used a fine mesh for forward modelling and a coarse mesh for the reconstruction itself.

The clinical study carried out by Ostermann was based on a small statistical sample as only 13 patients participated, meaning their positive results (false negative rate of 4/14, false positive rate of 3/11) could only provide a symbolic encouragement to researchers.

A similar study by Kerner et. al. on 26 subjects was conducted two years later on subject pre-classified using mammography [74]. A conclusion that spectroscopic data hold promise for the detection of malignancies was reached.

Investigation of clinical utility of the first-generation system was furthered by Soni, Hartov et. al. [120]. Images obtained from 18 normal and 24 abnormal subjects showed electrode and 3D artifacts, but it was still possible to visually distinguish between normal and abnormal subjects based on appearance of the images. The authors concluded consistently with previous research that raw admittivity data can be used to predict the presence of a malignancy through tissue dispersion behavior obtained from the spectroscopic aspect of the data.

The De Montfort MK2 system

A device for electrical impedance mammography was constructed at the De Montfort University, Leicester UK by Wang et. al. [131] called the De Montfort MK2 EIM system (1998). The device was able to collect complex measurements over the bandwidth 1 kHz - 5 MHz from a ring configuration of 32 electrodes embedded in a custom brassiere. Its electrodes were made of fabric and weaved into the brassiere which eventually posed problems in terms of contact impedance effects [122] (see section 3.1.2). Reconstruction of 2D slice through the breast was based on the back-projection methods developed at Sheffield. Authors of the apparatus encountered typical obstacles documented during the development of other impedance-tomographic devices, namely decreased resolution in the central region of the imaged body.

2.4.5 Full 3D reconstruction

The Dartmouth 3^{rd} generation system

After obtaining encouraging results from their tomographic device, the Dartmouth group continued with the development of an imaging system performing full 3D reconstruction. Based on the suggestions of a number of studies, i.e. Jossinet [70], it was proposed that the range of frequencies, the Dartmouth system collected measurements at, be expanded to at least 1 MHz and corresponding improvements were made to the system extending the frequency range to 12.5 MHz [55] marking the development of the third generation Dartmouth system (2008).

Previous to these efforts expansion to higher bandwidths has proven challenging, as the influence of parasitic effects on the performance of the circuitry grows [19].However, strength analysis has demonstrated the system had a signal-to-noise ratio (SNR) greater than 90 dB up to 7 MHz and 65 dB at 10 MHz.

This improved version of the system had 64 electrodes incorporated into a mechanical framework in multiple rings spaced at depth levels optimized for breast imaging. Activity of the levels was chosen appropriately for a given breast size. Furthermore, to eliminate skin-electrode contact considerations the Ag/AgCl electrodes of the device were coated with conductive gel, and prior to the examination, electrode contact impedances were measured and incorporated into the model. Patient specific finite-element meshes [90] were constructed from the measured array diameters customized for each patient and full 3D reconstruction was performed.

Recently, the Dartmouth third generation system was used to detect breast cancer via cyclic blood-volume changes in the chaotic vascular networks surrounding malignant tumours, employing time-difference imaging [54]. Nineteen women were examined using this technique which requires synchronicity of the system with pulse-oxymetry acquisition. Eight parameters establishing a link between the conductivity images and the pulse-oximeter signatures were extracted and inspected for diagnostic value. The maximum temporal correlation coefficient between the conductivity distribution and the pulse-oxymeter signals was found to provide the optimal discrimination with specifity of 81% and sensitivity of 77 %.

Rensselaer Polytechnical Institute ACT devices

Researchers at the previously mentioned Rensselaer Polytechnic Institute customized their ACT device for applications in breast EIT. The ACT3 (1994) was capable of applying independent currents to 32 electrodes and measure their respective voltages [38]. With it the group intended to imitate mammography geometry, where the breast is compressed by two opposing radioluscent plates. To achieve this, a test tank in the shape of a cube was constructed and electrodes were placed on two opposite faces of the tank each carrying a 4 by 4 array of square shaped electrodes.

An analytical solution to the forward model in this simplified homogenous mammography geometry, based on the separation of variables in the Laplace equation (valid while assuming homogenous conductivity distribution), was de-

veloped and verified experimentally [37].

To reconstruct the conductivity distributions, the body representing the rectangular box was broken down into cubical voxels, the conductivity of which was computed from a system of equations, derived from a discretization scheme approximating the first order term in the linearization of the conductivity distribution $\sigma = \sigma_0 + \eta$ [97].

The Rensselaer research group continued improving their earlier apparatus and as a result a successor, the ACT4 (2007), was introduced. The new version supported between 32 and 64 electrodes in both circular array and the opposing square configurations. Intended as a spectroscopic device, it has been designed to allow for data collection at frequencies from 3 kHz to 1 MHz.

The system performs reconstruction of distributions of the real and reactive parts of admittivity [87]. To investigate the utility of the device for breast cancer detection it was applied to the 'mammography' geometry discussed earlier [112], [72].

In cooperation with Cheju National University of Korea, the Rensselaer group also implemented the forward solver in the rectangular box geometry via the finite element method, adopting the Galerkin method on linear tetrahedral elements [62]. To tackle the inverse problem, the regularized one-step Gauss-Newton method was employed.

Duke University system

Researchers at the Duke University of North Carolina have constructed a 3D EIT system (2006) utilizing a cone shaped applicator designed to fit the breast to be imaged. The applicator contains a total of 128 electrodes mounted in seven layers [134].

To solve the inverse problem via an iterative scheme, the required forward computations were based on Spectral Element Method (SEM), whereas in other systems the forward calculation is usually enabled by an implementation of the Finite element method on linear elements. The Duke team chose to improve upon this by using higher order SEM with Gauss-Lobatto-Legendre basis functions and integration points [83].

An iterative solver is used to reconstruct the pulse-basis discretization of the difference between the current and a reference conductivity distribution [135]. On any given step of the iterative scheme, electric potential based on a current guess on the conductivity distribution is computed and a new guess is acquired using the regularized Gauss-Newton method entailing the minimization of a cost function representing the data misfit with an addition of a regularization term , yielding a system of equations solved by the conjugate gradients method.

The device was tested using both artificial phantoms and live subjects. Benchmark test on multiple artificial phantoms had been carried out and the device had been shown to offer SNR greater than 90 dB.

Sussex MK4 apparatus

The research group, which designed the De Montfort MK2 system, investigated the possibilities of 3D imaging by developing a full 3D reconstruction system at the University of Sussex - the Sussex MK4 apparatus (2014) [137].

This system employs a planar array of 85 electrodes at the bottom of a cylindrical tank attached under an examination table. The subjects lie prone and the examined breast is inserted into the tank. The electrodes themselves are slightly recessed from the array and conductive contact is provided by a saline solution as this was shown to reduce the contact impedance of the electrodes [111]. The electrode array is then pressed against the breast to minimize the depth of tissue examined.

An important innovation aimed at maximizing the number of independent measurements while maintaining good SNR is the arrangement of the planar array in a hexagonal pattern. When measurements are collected, the electrode array is subdivided into hexagonal areas where stimulations and measurements are carried out.

The finite element method is used to solve the forward problem and electrodes are introduced via the point electrode model, neglecting the contact impedance as the electrodes are not in direct contact with the breast.

During reconstruction, the sensitivity matrix (a matrix which relates perturbations in the boundary data to perturbations in the interior conductivity distribution) is iteratively updated to converge to the solution starting from an initial guess on the conductivity distribution. Advanced Tikhonov regularization techniques controlled by multiple regularization parameters are used.

Image analysis methods and optimization of the reconstruction algorithms for the MK4 system were considered in the thesis of G. Sze [122].

Figure 2.3: A graphical overview of breast EIT systems mentioned in this thesis. The devices are listed along with their most important features and references. Arrows signify influence the systems had on one another

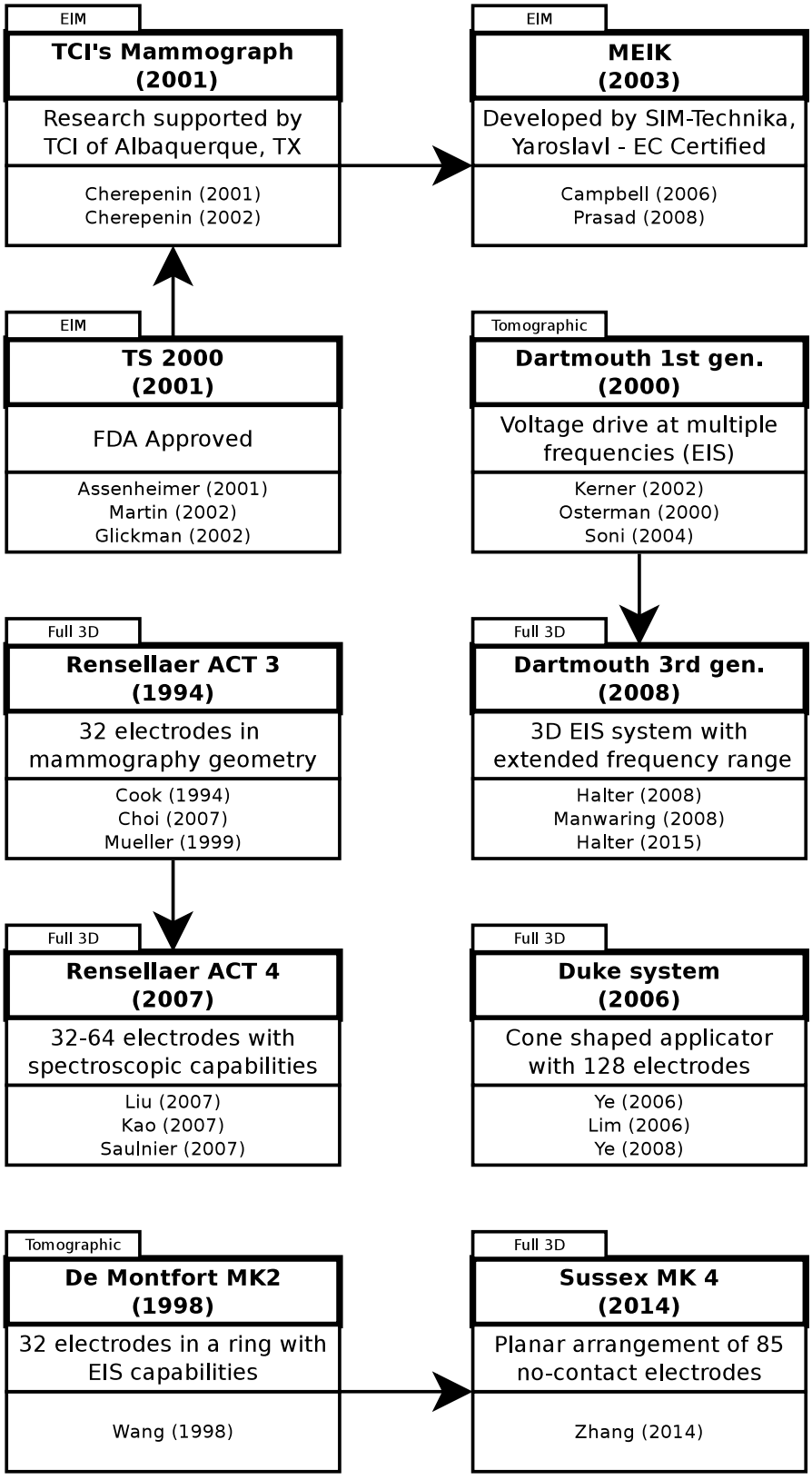

3. The Forward Problem

In many EIT systems, algorithms performing the reconstruction of conductivity distributions need to be able to compute voltage readings corresponding to a guess on the conductivity distribution the algorithm has at a particular moment during its runtime. This is usually the case when iterative techniques are employed. On each iteration, the solver's guess on the conductivity distribution is updated based on the misfit between corresponding voltage measurements on the boundary resulting from that distribution and the actual voltages acquired via physical instruments. To compute the boundary data, either analytical, or numeric models must be utilized and the search for an analytic model is only undertaken for simple geometries. For arbitrary shapes of the domain at interest, the Finite Element Method (FEM) is used. This chapter will outline the basic formulation of the problem in finite elements.

3.1 The mathematical model

In this section, theoretical description of the EIT problem will be derived from Maxwell equations assuming a quasistatic condition imposed by the time-harmonic nature of stimulating electric fields. Appropriate description of boundary conditions for practical models will be discussed.

3.1.1 Deriving the governing equations

The standard set of Maxwell equations in matter for a bounded domain $\Omega \subset \mathbb{R}^3$ (representing our body of interest) can be written in differential form as follows

$$\nabla \times \mathbf{E}(x,t) = -\partial_t \mathbf{B}(x,t) \tag{3.1}$$
$$\nabla \times \mathbf{H}(x,t) = \mathbf{j}(x,t) + \partial_t \mathbf{D}(x,t) \tag{3.2}$$
$$\nabla \cdot \mathbf{D}(x,t) = \rho(x,t) \tag{3.3}$$
$$\nabla \cdot \mathbf{B}(x,t) = 0 \tag{3.4}$$

where $x \in \Omega$ is a point in the body, $\mathbf{j}(x,t)$ represents the free current density while $\rho(x,t)$ denotes the free charge density. To complete the system, auxiliary fields, $\mathbf{D}$ - the displacement field and $\mathbf{H}$ - the magnetizing field, are defined as

$$\mathbf{D}(x,t) = \varepsilon(x)\mathbf{E}(x,t) = \varepsilon_0 \varepsilon_r(x)\mathbf{E}(x,t) \tag{3.5}$$
$$\mathbf{H}(x,t) = \frac{\mathbf{B}(x,t)}{\mu(x)} = \frac{\mathbf{B}(x,t)}{\mu_0 \mu_r(x)} \tag{3.6}$$

where $\varepsilon(x)$ is the permittivity of the material at a point x, ε_0 is the dielectric constant of free space and $\varepsilon_r(x)$ represents the spatial distribution of relative permittivity in the material. Similarly, $\mu(x)$ represents permeability, μ_0 is the permeability of free space and $\mu_r(x)$ is the relative permeability. Since we assume, that the material is linear and isotropic, both permittivity and permeability are scalar functions.

Furthermore, in a conductive body characterized by a conductivity distribution $\sigma(x)$, the free current density $\mathbf{j}(x,t)$ can be related to the electric field $\mathbf{E}(x,t)$ via Ohm's law

$$\mathbf{j}(x,t) = \sigma(x)\mathbf{E}(x,t) \tag{3.7}$$

Additionally, in case the electric field is time-harmonic with an angular frequency ω one can write

$$\mathbf{E}(x,t) = \mathbf{E}(x)e^{i\omega t} \tag{3.8}$$

resulting in the separation of spatial and temporal coordinates in the Maxwell equations consequently rewritten using 3.7, 3.8 as

$$\nabla \times \mathbf{E}(x) = -i\omega\mathbf{B}(x) \tag{3.9}$$

$$\nabla \times \mathbf{H}(x) = (\sigma(x) + i\omega\varepsilon(x))\,\mathbf{E}(x) \tag{3.10}$$

While the term, representing displacement current in equation 3.10, has to be taken into account (as shown in section 2.1.1), the induction term in the first equation can be safely neglected as tissues are mostly made up of water having relative permeability of almost 1. Consequently, if we restrict ourselves to simply connected domains, we have

$$\nabla \times \mathbf{E}(x) = 0 \implies \mathbf{E}(x) = -\nabla u(x) \quad x \in \Omega \tag{3.11}$$

where $u(x)$ is the scalar potential of the electric field. If we apply the divergence operator to equation 3.10 and express the electric field via the scalar potential as in equation 3.11, then since the divergence of a curl is always zero, we arrive at

$$\nabla \cdot (\gamma(x)\nabla u(x)) = 0 \quad x \in \Omega \tag{3.12}$$

where $\gamma(x) = \sigma(x) + i\varepsilon_0\varepsilon_r(x)\omega$ is the complex admittivity. Equation 3.12 is sometimes called Poisson's equation in EIT literature, which a recurring error. The equation should be called the continuum Kirchhoff's law and is a natural generalization of Laplace's equation.

3.1.2 Boundary conditions and electrode models

Furthermore, an issue that must be adressed is the specification of boundary conditions. In EIT, electrodes are attached to the body of interest which, according to a chosen stimulation pattern, supply current to the body or measure voltage response. To incorporate this into the physical description of the problem, a number of models can be used. The simplest model - the *continuum model*, prescribes current density on the boundary of the body while conservation of charge is satisfied and a choice of ground is made

$$\gamma\nabla u \cdot \mathbf{n} = \gamma\frac{\partial u}{\partial \mathbf{n}} = \mathbf{j}_i \quad \text{on} \quad \partial\Omega \tag{3.13}$$

$$\int_{\partial\Omega} \mathbf{j}_i \,\mathrm{d}S = 0 \tag{3.14}$$

$$\int_{\partial\Omega} u \,\mathrm{d}S = 0 \tag{3.15}$$

However, this model is not suitable for use with real experimental data because the current density at the boundary $\mathbf{j}_i$ is not known, as instead, we measure the current supplied by wires to discrete electrodes attached to the boundary.

To improve our description, we assume a constant current density over each electrode - the *gap model*. Yet both continuum and gap models give inaccurate results, because they fail to incorporate the shunting effect of the electrodes as the metal they are made of represents a low-resistive path for the current in itself [118].

Therefore, to account for the discreteness in a more suitable manner, we set the integral of the current density over a subset of the boundary corresponding to the surface of k-th electrode to the total amount of current it brings in

$$\int_{E_k} \gamma \frac{\partial u}{\partial \mathbf{n}} \, \mathrm{d}S = I_k \quad k = 1, 2, \ldots, N \tag{3.16}$$

$$\sum_{k=1}^{N} I_k = 0 \tag{3.17}$$

$$\gamma \frac{\partial u}{\partial \mathbf{n}} = 0 \quad \text{on} \quad \partial\Omega / \bigcup_{k=1}^{N} E_k \tag{3.18}$$

assuming the electrodes are perfect conductors, we complete the so called *shunt model* by including the following condition

$$u = U_k \quad \text{on} \quad E_k \quad k = 1, 2 \ldots, N \tag{3.19}$$

$$\sum_{k=1}^{N} U_k = 0 \tag{3.20}$$

which means we assume the potential is constant on each electrode. It has to be noted, that in an experimental environment, U_k are not a priori known as they are the results of measurements as opposed to the magnitude of stimulation currents. Equation 3.17 represents the charge conservation law and ensures the existence of a solution while 3.20 specifies the choice of ground and is needed to guarantee the uniqueness of the solution [118].

However, even the shunt model does not give accurate predictions in an experimental environment. It overlooks an electrochemical effect that occurs between the surface of the electrode and the body - the formation of a resistive layer between the electrode and the skin. This effect was experimentally verified by Cheng et. al. [34] and an improvement to the shunt model was made by accounting for the voltage drop on the electrodes - a feature of the *complete electrode model*.

$$u + Z_k \gamma \frac{\partial u}{\partial \mathbf{n}} = U_k \quad \text{on} \quad E_k \quad k = 1, 2, \ldots, N \tag{3.21}$$

Where Z_k represents the contact impedance of the kth electrode. Existence and uniqueness of the electric potential u has been shown for this model by Somersalo et. al. [118] and it has been demonstrated that it predicts experimental measurements with precision better than 0.1%.

3.2 Numerical solution of the forward problem

This section will discuss the means of performing the EIT forward calculation on a computer. The EIDORS software (section 1.4) package was chosen as a stepping stone for outlining all the necessary components of the calculation, and parts of its original implementation will be discussed.

In order to solve the EIT forward problem numerically, the governing model has to be discretized using a suitable scheme. First of all, to employ the finite element method [25], a weak formulation of the problem [42] has to be derived and discretized based on the restriction of function spaces involved to their discrete subspaces - the Galerkin method.

3.2.1 Deriving the weak formulation

First and foremost, we gather all the equations comprising the complete electrode model we arrived at in the last section

$$\nabla \cdot (\gamma(x)\nabla u(x)) = 0 \quad x \in \Omega \tag{3.12}$$

$$\int_{E_k} \gamma \frac{\partial u}{\partial \mathbf{n}} \, \mathrm{d}S = I_k \quad k = 1, 2, \ldots, N \tag{3.16}$$

$$u + Z_k \gamma \frac{\partial u}{\partial \mathbf{n}} = U_k \quad \text{on} \quad E_k \quad k = 1, 2, \ldots, N \tag{3.21}$$

$$\gamma \frac{\partial u}{\partial \mathbf{n}} = 0 \quad \text{on} \quad \partial\Omega / \bigcup_{k=1}^{N} E_k \tag{3.18}$$

$$\sum_{k=1}^{N} I_k = 0 \tag{3.17}$$

$$\sum_{k=1}^{N} U_k = 0 \tag{3.20}$$

To derive the weak formulation of the problem for an unknown function $u \in V$, where V is a function space ensuring the correctness of the subsequent mathematical reasoning (a Sobolev space [42]), we start with 3.12 by multiplying both sides of the equation by a test function $v \in \hat{V}$ (in the complex case we multiply by the complex conjugate v^*), where $\hat{V}$ is also a suitable function space, and integrating over Ω

$$\int_{\Omega} \nabla \left(\gamma \nabla u\right) v \, \mathrm{d}x = 0 \quad \forall v \in \hat{V} \tag{3.22}$$

By utilizing Green's identity and the Gauss-Ostrogradsky theorem we have

$$\begin{aligned} \int_{\Omega} \nabla \cdot (\gamma \nabla u v) \, \mathrm{d}x &= \int_{\partial\Omega} \gamma (\nabla u) v \mathbf{n} \, \mathrm{d}S \\ &= \int_{\Omega} \nabla \cdot (\gamma \nabla u) \, v \, \mathrm{d}x + \int_{\Omega} \gamma \nabla u \cdot \nabla v \, \mathrm{d}x \quad \forall v \in \hat{V} \end{aligned} \tag{3.23}$$

Thus 3.22 can be rewritten as

$$\int_{\Omega} \gamma \nabla u \cdot \nabla v \, \mathrm{d}x = \int_{\partial\Omega} \gamma \frac{\partial u}{\partial \mathbf{n}} v \, \mathrm{d}S \quad \forall v \in \hat{V} \tag{3.24}$$

Equation 3.24 is the weak formulation of the problem. The benefit of the weak formulation lies in the fact, that the solution no longer has to satisfy classical regularity conditions, instead, its derivatives are only required to exist in the sense of distributions. Without this generalization of the notion of a solution - every classical solution being a weak solution, it would not be possible to discretize the problem using piecewise linear functions, the derivatives of which do not exist in the classical sense.

3.2.2 Discrete approximation of the problem

To adopt the Galerkin method, we restrict ourselves to subspaces $V_h \subset V$, $\hat{V}_h \subset \hat{V}$ having finite bases - the trial $\{\phi_i\}_{i=1}^n$ and test basis $\{\hat{\phi}_i\}_{i=1}^n$.

Assume we have a finite element mesh consisting of p tetrahedral elements and n vertices (degrees of freedom) at our disposal. For both the trial and test basis, piecewise linear functions with limited support are chosen

$$\phi_i(x) = \begin{cases} 1 & \text{on vertex } i \\ 0 & \text{otherwise} \end{cases} \tag{3.25}$$

The weak solution u_h can be expressed in terms of the trial space basis as follows

$$u_h = \sum_{i=1}^{n} u^i \phi_i \tag{3.26}$$

where u_i is the value of the electrical potential at node i.

Thus equation 3.24 can be rewritten using decomposition into the trial and test bases as

$$\sum_{j=1}^{n} u^j \int_\Omega \gamma \nabla \phi_j \nabla \hat{\phi}_i \,\mathrm{d}x = \int_{\partial\Omega} \gamma \frac{\partial u_h}{\partial \mathbf{n}} \hat{\phi}_i \,\mathrm{d}S \quad \forall i = 1, 2, \ldots, n \tag{3.27}$$

Let us now examine an element $\Omega_l \subset \Omega$ which shares one of its triangular faces $F_l \subset \partial\Omega_l$ with the electrode E_k as depicted in figure 3.1.

To outline the form of local relations implied by 3.27, we examine one such relation for a fixed test function $\hat{\phi}_{n_1}$, the support of which extends to neighboring element nodes p_1, n_2, n_3 as depicted by figure 3.1b (shaded area). It has to be noted, that the third dimension was intentionally truncated in figure 3.1b and that there are additional nodes connected with n_1 outside the depicted plane.

Thus by setting $i = n_1$ (see figure 3.1) and substituting for the normal derivative at the right-hand side of equation 3.27 from the boundary condition 3.21, we arrive at

$$\sum_{j \in J_{n_1}} u^j \int_{S_{n_1}} \gamma \nabla \phi_j \nabla \hat{\phi}_{n_1} \,\mathrm{d}x = \int_{\partial\Omega \cap S_{n_1}} \frac{1}{Z_k} \left(U_k - u_h\right) \hat{\phi}_{n_1} \,\mathrm{d}S \tag{3.28}$$

For the sake of formula simplicity, we have adopted the following notation in the equation above - $J_{n_1} = \{j \in \mathbb{N} \mid \operatorname{supp} \phi_j \cap \operatorname{supp} \hat{\phi}_{n_1} \neq \emptyset\}$, $S_{n_1} = \operatorname{supp} \hat{\phi}_{n_1}$. A careful reader will notice, that, as currently defined, the index set J_{n_1} includes indices of trial functions for which the measure of $\operatorname{supp} \phi_j \cap \operatorname{supp} \hat{\phi}_{n_1}$ is zero in $\mathbb{R}^3$ (the supports of these function 'share a face' or 'share an edge'). To correct

Figure 3.1: Illustration of a boundary mesh element Ω_l and an example of how it may form a part of the kth electrode surface

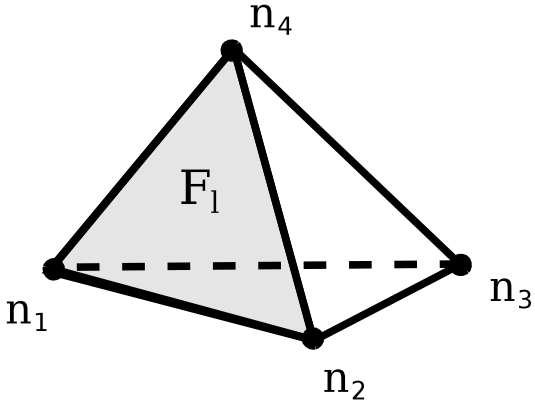

(a) A tetrahedral element Ω_l, F_l represents its face, which is in contact with the electrode E_k

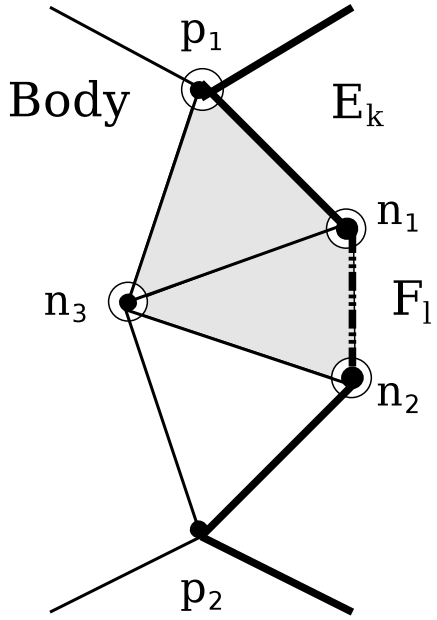

(b) The same element contributing one of its faces F_l to the surface of the kth electrode E_k. The color fill highlights the support of the test function $\hat{\phi}_{n_1}$. The third dimension is truncated.

the definition, we add the condition that this set does not include such indices. By the support of a function we mean the following set

$$\operatorname{supp}\varphi = \overline{\{x \in \mathbb{R}^3 \mid \varphi(x) \neq 0\}} \tag{3.29}$$

After plugging in for u_h at the right-hand side and rearranging the equation we rewrite 3.28 as

$$\sum_{j \in J_{n_1}} u^j \left(\int_{S_{n_1}} \gamma \nabla \phi_j \nabla \hat{\phi}_{n_1} \,\mathrm{d}x + \int_{\partial\Omega \cap S_{n_1}} \frac{1}{Z_k} \phi_j \hat{\phi}_{n_1} \,\mathrm{d}x \right) = \int_{\partial\Omega \cap S_{n_1}} \frac{1}{Z_k} U_k \hat{\phi}_{n_1} \,\mathrm{d}S \tag{3.30}$$

There are two additional relationships a degree of freedom might have with the boundary of the body. One of such situations arises for a node such as p_1 (figure 3.1), where $\operatorname{supp}\hat{\phi}_{p_1} \cap \partial\Omega$ splits into two subsets - one where condition 3.21 is satisfied, while 3.18 holds at the other. In this case, the right hand side of 3.28 is modified accordingly.

Secondly, if instead, we had chosen a node not interacting with the boundary degrees of freedom at all, or a boundary node satisfying 3.18 on the whole intersection of its corresponding test function support and the body boundary, the right hand side of 3.28 would have been zero

In general, the surface of the electrode E_k will consist of a certain number m of element faces $\{F_l\}_{l=1}^m$. These are bound by the condition 3.16 further expanded

as follows

$$\begin{aligned} I_k = \int_{E_k} \gamma \frac{\partial u_h}{\partial \mathbf{n}} \,\mathrm{d}S = \int_{E_k} \frac{1}{Z_k} (U_k - u_h) \,\mathrm{d}S = \sum_{l=1}^{m} \int_{F_l} \frac{1}{Z_k} (U_k - u_h) \,\mathrm{d}S \\ = \frac{1}{Z_k} U_k |E_k| - \sum_{l=1}^{m} \sum_{j \in J_l} u^j \int_{F_l} \frac{1}{Z_k} \phi_j \,\mathrm{d}S \end{aligned} \tag{3.31}$$

Where we introduce $J_l = \{j \in \mathbb{N} \mid F_l \cap \operatorname{supp} \phi_j \neq \emptyset\}$, $|E_k|$ denoting the surface measure of E_k.

Finally a global full-rank linear system is assembled from the 'local' equations of the form 3.28.

For example, in the original (2002) implementation of EIDORS code [107] a global system is derived, consisting of block matrices $A_M \in \mathbb{C}^{n \times n}$, $A_Z \in \mathbb{C}^{n \times n}$, $A_V \in \mathbb{C}^{n \times N}$, $A_D \in \mathbb{C}^{N \times N}$, global vector of nodal potential values $\mathbf{u} \in \mathbb{C}^n$, electrode voltage readings $\mathbf{U} \in \mathbb{C}^N$ and the corresponding stimulation current pattern $\mathbf{I}$ (satisfying the charge conservation law 3.17) taking on the following form

$$\begin{bmatrix} A_M + A_Z & A_V \\ A_V^T & A_D \end{bmatrix} \begin{bmatrix} \mathbf{u} \\ \mathbf{U} \end{bmatrix} = \begin{bmatrix} 0 \\ \mathbf{I} \end{bmatrix} \tag{3.32}$$

The block matrix on the left-hand side is called the admittivity matrix, or the system matrix. Respectively, the block components of the first row A_M, A_Z, A_V correspond to the expressions in equation 3.28, while the constituents of the second row reflect equation 3.31.

3.2.3 Solving the linear system

To characterize the linear system, a general discussion of the admittivity matrix properties is in order. As a consequence of the limited support of the test and trial functions (equation 3.25), the matrix is sparse. Moreover, it is square, symmetric and full-rank.

In the subsequent discussion, we use simple notation for the linear system 3.32, with the index n now representing the total number of rows of the admittivity matrix.

$$Au = b \quad A \in \mathbb{R}^{n \times n} / A \in \mathbb{C}^{n \times n} \quad u, b \in \mathbb{R}^n / u, b \in \mathbb{C}^n \tag{3.33}$$

Approaches to its solution can be divided into two main classes - direct and iterative. An another aspect influencing the choice of a suitable algorithm is whether we are dealing with complex or real physical quantities.

This section will discuss the methods N. Polydorides chose for his original implementation of EIDORS3D [107] It has to be noted that, as of today, EIDORS3D v.3 uses a different implementation of the forward solver by A. Adler (2005) as a default option. However, technical documentation, detailing the means of the operation of its components, is not provided by the authors. The EIDORS website merely provides raw source code with occasional comments for functions [2].

If the system matrix is real, it is also positive definite, thus it is suitable for a direct solution using the Cholesky decomposition, while LU decomposition is employed in the direct complex case.

Polydorides argued, that iterative solvers are much more efficient at solving the linear system, since the direct methods refine the solution to an unnecessary

degree of precision. Needlessly accurate calculation of a solution to the linear system is redundant, since the system is a result of a discrete approximation to a continuous problem, which introduces discretization error into the model.

The original implementation of EIDORS3D offers the ability to solve the linear system iteratively using Preconditioned Conjugate Gradients (PCG) in the real case.

If the entries of the system matrix are complex, the ideas behind the CG method may be extended to cases, where A is not positive definite. One such algorithm is the Bi-Conjugate Gradients (BiCG) method [52] used by the original implementation of EIDORS3D to deal with the complex admittivity case iteratively.

All of the methods for solving the linear system 3.33 mentioned in this section are provided by the standard Matlab toolkit [3] the EIDORS3D package is built upon. Table **??** summarizes the discussion of choosing appropriate linear system solvers for given characteristics of the admittivity matrix.

Table 3.1: Means of solving the linear system with their corresponding Matlab functions in parentheses. For the conjugate gradient methods, preconditioners in the form of incomplete decompositions are used. Furthermore, when applying the **mldivide** function to a matrix in Matlab, its properties are determined automatically and a suitable solver is called.

	Direct	Iterative
Real	Cholesky (**mldivide**)	PCG (**cholinc** → **pcg**)
Complex	LU (**mldivide**)	BiCG (**luinc** → **bicgstab**)

3.2.4 Mesh refinement considerations

In the context of EIT, H. Dehghani & M. Soleimani evaluated the amount of error introduced into the forward computation by using a discrete approximation of the problem by conducting a numerical experiment [41]. Control over the discretization error is important, since it may cause image artifacts in systems, where the inverse solver relies upon the ability to compute voltages for a particular admittivity distribution.

The authors investigated the influence of mesh refinement on the discretization error by comparing the computed electrical fields between seven meshes of an ellipsoid approximating a breast of an increasing degree of refinement with the finest mesh selected as referential.

It was concluded, that the largest error occurs in the regions under each electrode where the gradient of the electric potential is the largest. This suggests, that the parts of the volume close to an electrode need to be treated with special care in FEM meshing.

Furthermore, anomalies were introduced into the model body and the errors were recalculated. Along with the previously observed effects, inaccuracies near the boundaries of the implanted anomalies were detected. These may be explained by the same logic as the near-electrode errors - at an interface between the homogenous background and an anomaly, the gradient of the electric potential is also very high. This is of great importance to the development of reconstruction

algorithms, as the high sensitivity of the EIT inverse problem to measurement errors has a great deal of influence on the quality of images produced by the method.

To prove that mesh refinement considerations are reasonable, Molinari et. al. compared discretization error estimates for finite element meshes with uniform refinement to meshes refined by a self-adaptive algorithm [95], [94]. Molinari concluded, that by employing such a technique, it is possible to substantially reduce the number of nodes required to obtain an image reconstruction with the same degree of accuracy than by performing uniform refinement.

EIT researchers agree, that the reconstruction process is also sensitive to inaccuracies in the geometry of the actual imaged body and electrode placement [18] which often causes image artifacts to present themselves. To tackle this problem in the area of breast EIT, Forsyth et. al. developed methods for optical breast shape capture, allowing for he construction of patient-specific finite element meshes along with ensuring proper electrode representation. The researchers successfully tested their ideas on an artificial phantom and a female volunteer [44]. This may prove very useful, since given the significant variations in breast size and shape among women, the design of an optimally-shaped scanner is challenging.

The EIDORS software package offers the possibility of working with arbitrary geometries of the body at interest due to its extensible design. IT allows the user to construct both forward and inverse model structures from an arbitrary FEM mesh generated by Netgen software [113].

3.3 Optimal stimulation patterns

To maximize the efficiency of data collection by an EIT system, suitable stimulation current patterns have to be chosen.

Even though the mathematical model is linear, applying any linearly independent combination of current patterns does not allow for the construction of an arbitrary pattern by their combination [33]. One of the reasons for this is the fact that the voltage response to a particular stimulus cannot be measured with absolute accuracy and a part of the information to be extracted is lost introducing a nonlinearity.

To choose a current pattern means to select a subset of electrodes available to the system and drive prescribed currents (assuming the device was constructed so as to operate in current drive mode) through these electrodes, while condition 3.17 is satisfied.

Numerous aspects of the EIT problem need to be considered before making such a choice. First of all, the voltage response to a particular stimulus serves as a source of information to the image reconstruction process, therefore, we naturally aim to maximize the amount of information we can extract from a set of voltage measurements corresponding to the drive current sequence. However, this problem is constrained by speed and simplicity of hardware. A system with a large number of electrodes could, in theory, provide more information than a simpler system. However, switching of its circuitry it would consume more time and its hardware would be more susceptible to parasitic effects.

3.3.1 Early approaches & pair-drive patterns

The earliest patterns utilized by EIT systems are *adjacent* and *opposite* patterns, jointly referred to as pair-drive. When the adjacent pattern is employed, the system drives current through adjacent electrodes sequentially while collecting measurements at an another selection (i.e at all other electrodes). Adjacent patters were the first stimulation currents employed in an EIT system - the Sheffield Mk1 [26].

In a number of applications, adjacent patterns are deemed inefficient as they only partially penetrate insulative barriers surrounding the conductive body, i.e. in brain imaging [124]. This was one of the reasons opposite pair-drive patterns came to be considered. In this configuration, the device drives current patterns through a sequence of opposing electrodes.

Avis & Barber investigated the advantages of using opposite drive compared to adjacent and concluded that, while adjacent patterns offer better image resolution (determined by comparing the condition of the Sheffield back-projection algorithm reconstruction matrix for both cases), opposite patterns outperform the adjacent in terms of voltage measurement SNR [12].

3.3.2 Distinguishability and further development

Notions of distinguishability of conductivity distributions by different current patterns were given rigorous mathematical treatment by D. Isaacson [65]. He worked with the continuum model 3.13 (often preferred in theoretical calculations) and defined distinguishability of two conductivity distribution as follows.

Two conductivity distributions σ_1, σ_2 inside a domain Ω are considered disinguishable by measurement of precision ε if there exists a current density $\mathbf{j}$ for which $\|\mathbf{j}\| = 1$ and

$$\|V(\cdot, \sigma_1, \mathbf{j}) - V(\cdot, \sigma_2, \mathbf{j})\| > \varepsilon \tag{3.34}$$

where V denotes the restriction of $u(x)$ to the boundary and $\|\cdot\|$ is the L^2 norm

$$\|f\|^2 = \int_{\partial\Omega} |f|^2 \, \mathrm{d}S \tag{3.35}$$

In this formalism, Isaacson considered the current density that best distinguishes between σ_1 and σ_2 to be

$$\mathbf{j_{opt}} = \arg\max_{\|\mathbf{j}\|=1} \|V(\cdot, \sigma_1, \mathbf{j}) - V(\cdot, \sigma_2, \mathbf{j})\| \tag{3.36}$$

Furthermore, an operator defined implicitly by $A(\sigma)\mathbf{j} = V(\cdot, \sigma, \mathbf{j})$ is studied and Isaacson continues by showing the best current densities are eigenfunctions of the operator $(A(\sigma_2) - A(\sigma_1))$ corresponding to its highest eigenvalues. Thus the best current to distinguish between σ_1 and σ_2 is given by

$$\max_{\|\mathbf{j}\|=1} \|(A(\sigma_2) - A(\sigma_1))\mathbf{j}\| = |\lambda_1| \tag{3.37}$$

with $(\mathbf{j_1}, \lambda_1)$ being the eigenpair with the largest eigenvalue.

To present an example, he performed the calculations above in two dimensions for a disk of homogenous conductivity σ in the center of a disk domain (of radius 1)

which was also considered homogenous with conductivity set to unity. In order to distinguish this model distribution from an absolutely homogenous one, he found that the space of optimal eigenfunctions is spanned by the functions $C\cos(\theta)$, $C\sin(\theta)$, where θ is the azimuth and C is a constant - the so called *trigonometric patterns*. What's more, he gave an estimate of the smallest detectable object in this configuration.

Isaacson later expanded his study with the help of M. Cheney to the discrete case (the shunt model) [32]. In this situation, the norms in the definition of distinguishability are replaced with their discrete ℓ^2 analogues. The authors also considered a slightly adjusted notion of distinguishability taking the total power dispersed within the body into account. Discriminating current patterns in terms of power is necessary as some ranked high by the old definition may not satisfy safety requirements. When normalising by total power dispersed assuming the distribution σ_1 we have

$$\delta_p(\sigma_1, \sigma_2, \mathbf{j}) = \sqrt{\frac{\sum_{k=1}^{N} |V_1^k - V_2^k|^2}{\mathfrak{Re}\left(\sum_{k=1}^{N} I_k (V_1^k)^*\right)}} \tag{3.38}$$

In the discrete case, Walsh [32][133], adjacent, opposite and trigonometric current patterns were compared in terms of size of the smallest distinguishable object in the cocentric disk configuration with Walsh and trigonometric patterns performing superior to simple pair drive patterns.

More recent results were presented by Adler et. al. [8]. His team proposed a different distinguishability measure than Isaacson and compared various choices of stimulation patterns on its basis. After carrying out simulations in a 2D circular body surrounded by 16 electrodes, the authors concluded that the traditional adjacent current patterns perform poorly compared to trigonometric patterns and pair-drive patterns where the angular separation of the source pair is greater than 90°.

On the other hand, apart from reaching the general conclusion that the EIT problem is very sensitive towards forward modeling error in static imaging[1] (contact impedances, electrode sizes, electrode locations and the boundary shape of the object) Kolehmainen et. al., showed that the adjacent stimulation pattern is less susceptible to these uncertainties than the trigonometric one [80].

[1] A variant of EIT where one aims to reconstruct the absolute magnitude of the admittivity distribution. Its counterpart - difference imaging, can be employed to suppress the effect of these errors to some degree

4. The Inverse Problem

Over the years of EIT research, the reconstruction of an admittivity distribution within a physical body from voltage measurements collected at its boundary has proven to be challenging. The solution of this inverse problem is certainly the most important topic in EIT research and attracts theoreticians and experimentators alike. There is a number of research works, namely doctoral theses, offering broad coverage of the problem [107, 20, 50, 33, 23, 127, 84, 61]. In order to provide a reliable imaging modality for various applications discussed in the first chapter, namely medical imaging, there are many aspects of the inverse calculation to be considered.

When attempting to implement a numerical solution, especially those based on linearisation, to the inverse problem the main obstacle that has to be overcome is the *ill-posedness* of the problem. Unfortunately, it is difficult to give an all-encompassing characterization of an ill-posed inverse problem. In essence, the problem suffers from a shortage of information preventing its naive solution by simple inversion. For example, to solve the problem numerically, at some point we arrive at a linear system, whose coefficient matrix exerts a large condition number. Usually, we avoid solving such problems and attempt to improve the underlying mathematical model. However, there are certain situations, where the coefficient matrix is *ill-conditioned* in its true form and this is an intrinsic property of the problem. In such cases, obtaining a stable solution of the problem requires treatment in terms of advanced numerical methods i.e by the means of *regularization* [56].

In practice, the ill-conditioning of the EIT problem implies that there is no direct 'classical' approach to inverting the forward calculation and without the help of regularization, the reconstruction process would almost certainly return useless images. Additionally, the above difficulties also render the problem sensitive to both model and data errors, resulting in the problem being considered ill-posed in Hadamard's sense.

Before attempting to solve an ill-conditioned problem, it is important to determine what kind of ill-conditioning to expect and whether there is any prior information which can be used to remedy the deficiency. Furthermore, there are a number of numerical regularization methods both direct and iterative in nature, that have been considered for EIT image reconstruction, each having its advantages depending on the approach taken to the formulation of the inverse problem.

4.1 A theoretical point of view

The inverse admittivity problem was first subjected to rigorous mathematical treatment by A. P. Calderón in 1980 [29] and later came to be referred to as the Calderón's problem. He asked, whether one can uniquely determine the electrical conductivity of a medium by making voltage or current measurements at its boundary. To answer this question, while working with the continuum model, he

studied the Dirichlet-to-Neumann mapping (DtN)

$$\Lambda_\gamma \left(u\big|_{\partial\Omega} \right) = \left(\frac{\partial u}{\partial \mathbf{n}} \right) \Big|_{\partial\Omega} \tag{4.1}$$

To investigate the inverse problem - determining γ knowing Λ_γ, Calderón studied the properties of the following quadratic form

$$Q_\gamma(u\big|_{\partial\Omega}) \coloneqq \int_\Omega \gamma |\nabla u|^2 \, \mathrm{d}x = \int_{\partial\Omega} \Lambda_\gamma(u\big|_{\partial\Omega}) u\big|_{\partial\Omega} \, \mathrm{d}S \tag{4.2}$$

which can be interpreted as a measure of energy required to maintain the potential $u\big|_{\partial\Omega}$ at the boundary.

This problem was later found related to the Schrödinger equation and several results were proved by Sylvester & Uhlmann, namely the uniqueness of solution with complete boundary data in the isotropic case [121]. As in practice, the data is only known on a part of the boundary, the partial data problem was considered by a number of researchers [73, 99, 63]. A general overview of the whole topic is given by Uhlmann in [126].

4.2 The basic ideas of regularization

4.2.1 Ill-conditioned systems of equations

To outline the underlying principles of regularization, consider a least-squares problem

$$x_{LS} = \min_{x \in \mathbb{C}^n} \|Ax - b\| \tag{4.3}$$

where the singular values $\{\sigma_j\}_{j=1}^r$ of the coefficient matrix $A \in \mathbb{C}^{m \times n}$ of rank r are inconveniently distributed giving rise to a high condition number of the matrix. There are two main classes of this vague characterization - rank-deficiency and discrete ill-posedness [56].

Rank-deficient problems are characterized by the presence of a clear gap between large and small singular values in the coefficient matrix singular value spectrum, which can be interpreted as a near linear-dependence of a number of its rows. Therefore, the matrix can be seen as containing an amount of redundant information and the basic strategy to condition such matrices is to extract the linearly independent part by the means of truncation of its singular value decomposition (SVD) - the Truncated Singular Value Decomposition method (TSVD).

If there is no well-defined gap in the singular value spectrum of the coefficient matrix and the singular values decay gradually to zero, we are dealing with a discrete ill-posed problem. For example, a notorious occurrence of such problems is in the discretization of Fredholm integral equations of the first kind. To deal with such cases, a trade-off between the norm of the residual and size of the solution has to be made, where the notion of size of the solution is specific to the regularization strategy employed.

4.2.2 The influence of noise and how to suppress it

Suppose, that the right-hand side of 4.3 is contaminated by a noise vector $\tilde{b}$

$$b = b_e + \tilde{b} \tag{4.4}$$

where b_e is the exact vector and $\|b_e\| \gg \|\tilde{b}\|$. If we attempt to compute the naive solution

$$x_n = A^\dagger b = \sum_{j=1}^{r} \frac{u_j^* b_e}{\sigma_j} v_j + \sum_{j=1}^{r} \frac{u_j^* \tilde{b}}{\sigma_j} v_j \tag{4.5}$$

we will find it overwhelmed by noise even though its norm is significantly smaller. This is because while the first sum corresponds to the exact solution x_e we would like to obtain, the second sum represents the projection of the noise vector into the left singular basis of A and the influence of these components is amplified by the presence of the singular values in the denominators.

Therefore, we seek to modify the least squares problem 4.3 in a way that reduces the influence of noise on its solution. If the problem is merely rank-deficient we opt for TSVD, that is extracting k terms of its dyadic expansion, where k is an example of a *regularization parameter* usually chosen to be the numerical rank of the coefficient matrix.

There are a number of strategies we could employ in the discrete ill-posed case, for example, the Tikhonov regularization scheme is of the form

$$x_T = \arg\min_{x \in \mathbb{C}^n} \{ \|Ax - b\|^2 + \lambda^2 \Omega(x)^2 \} \tag{4.6}$$

Where λ is a regularization parameter controlling the influence of the added term on the least squares problem. The functional $\Omega(x)$ is called the *discrete smoothing norm* and is usually chosen such that

$$\Omega(x) = \|Lx\| \tag{4.7}$$

with L either being the identity matrix, a diagonal weighting matrix or a discrete approximation of a derivative operator and each choice represents a form of bias - giving preference to solutions with smaller norms or smoother solutions respectively. In this case, the solution can be expressed as

$$x_T = \left(A^* A + \lambda^2 L^* L) \right)^{-1} A^* b \tag{4.8}$$

Furthermore we can include a bias toward an a priori estimate on the desired solution x_p

$$\Omega(x) = \|L(x - x_p)\| \tag{4.9}$$

The procedure could also be augmented with statistical a-priori information in the form of covariance matrices to obtain the generalized Tikhonov solution and doing so has a probabilistic interpretation [71]. If the errors in the right-side b are correlated and $Q^{1/2} b$ represents its de-correlation, we modify the problem in the following way

$$x_{GT} = \arg\min_{x \in \mathbb{C}^n} \{ \|Ax - b\|_Q^2 + \|x - x_p\|_P^2 \} \tag{4.10}$$

Where $\|x\|_M^2 = x^* M x$ and $P = L^* L$.

4.3 Numerical solution to the inverse problem

The standard way of approaching the EIT inverse problem is via the *output least squares* method which is characterized by seeking a solution of the form

$$\arg\min_{\gamma\in\mathbb{C}^p} \|U_m(I_j) - F(\gamma, I_j)\| \quad \forall I_j \in \{I_1, \ldots, I_d\} \tag{4.11}$$

Where $U_m \in \mathbb{C}^N$ is a vector of measured electrode voltages, $I_j \in \mathbb{C}^N$ is the j^{th} stimulation pattern and $F(\gamma, I_j)$ is the nonlinear *forward operator* relating a conductivity distribution to electrode potential values. This method can be interpreted as follows - the solution to this problem minimizes the misfit between the actual observed voltages and those corresponding to the solution.

4.3.1 Introducing regularization

Without a direct nonlinear approach to solving 4.11 the algorithm has to rely on linearisation eventually. In his doctoral thesis, W.R. Breckon showed that both the nonlinear problem and its linearization are ill-posed [23]. This gives rise to a natural question. Do we regularize the underlying non-linear problem to cure the ill-posedness, or do we condition the result of linearisation? This opens up a wide range of possibilities of treating the EIT inverse problem in terms of regularization strategies.

Simple minimization in 4.11 will not lead to useful results. Breckon showed on a simple example, that a minimum for this rudimentary cost function lies in a long narrow valley. To obtain a meaningful solution the problem is modified much like in the case of ill-conditioned linear systems

$$\arg\min_{\gamma\in\mathbb{C}^p}\{\|U_m(I_j) - F(\gamma, I_j)\|^2 + \lambda^2\Omega(\gamma)^2\} \quad \forall I_j \in \{I_1, \ldots, I_d\} \tag{4.12}$$

A typical choice for the smoothing norm in EIT is

$$\Omega(\gamma) = \|L(\gamma - \gamma_p)\| \tag{4.13}$$

where L is a discrete approximation of a differential operator and γ_p is an a priori estimate on the admittivity distribution obtained i.e by mapping known anatomical features. The matrix L could be chosen to approximate the Laplacian on piecewise constant functions [108], a first order differential operator or the inverse Gaussian smoothing filter (an 'infinite' order differential operator)[22].

Imposing any a priori smoothness will naturally represent a penalty to distributions with sharp edges. One way of allowing the reconstruction of discontinuities is by setting the penalty term $\Omega(\gamma)$ to the Total Variation (TV) functional [20, 21, 50], which takes the following form for non-differentiable functions

$$TV(\gamma) = \sup_{\mathbf{v}\in\mathcal{V}} \int_\Omega f\nabla\cdot\mathbf{v}\,\mathrm{d}x \tag{4.14}$$

where $\mathcal{V}$ is the space of continuously differentiable normed vector-valued functions that vanish on $\partial\Omega$.

An another strategy might be chosen when we can impose a number of constraints for the admittivity distribution, restricting our search to a subset of the set of all admissible distributions - the Subspace Regularization Method (SSRM) [127, 129].

4.3.2 Approaches to the inverse calculation

There are three 'refinement' stages of EIT reconstruction methods - algorithms based on linearisation, nonlinear iterative techniques finding analogy in the Newton-Rhapson method and last but not least fully nonlinear approaches.

The simplest way to perform the inverse calculation is by linearising the forward operator around a particular admittivity γ_0

$$F(\gamma) \approx F(\gamma_0) + J(\gamma - \gamma_0) \tag{4.15}$$

Where J is the Jacobian of the forward operator calculated at point γ_0. If we define $\Delta\gamma = \gamma - \gamma_0$ and $\Delta U = U_m - F(\gamma_0)$, then for the choice of regularization in 4.13 the solution can be expressed as [123]

$$\Delta\gamma = \left(J^*J + \lambda^2 L^*L\right)^{-1}\left(J^*\Delta U + \lambda^2 L^*L(\gamma_p - \gamma_0)\right) \tag{4.16}$$

A well-established example of an algorithm relying on a single Tikhonov regularized solution is NOSER [31, 33].

Using a single Tikhonov regularized step is valid for small changes and is often seen in *difference imaging* where the goal is to produce i.e. a temporal succession of images where occurring changes are expected to be small. Difference imaging (Dynamical EIT) was studied in the thesis of M. Vauhkonen [127] with special focus on reconstruction speed while recently, a nonlinear approach to difference imaging was considered by Liu et. al. [86].

A more sophisticated approach is by designing an iterative process which progresses towards the solution by calculation of the Jacobian at each step in analogy with the multi-variable Newton-Rhapson method approximated by the Gauss-Newton method, which neglects all but the first order terms in the expansion of $F(\gamma, I_j)$, with the addition of regularization or modification to arrive at the Levenberg-Marquardt method [91, 107, 108].

Finally, fully nonlinear methods for image reconstruction have been considered mostly based on the theoretical foundations to the inverse conductivity problem described in section 4.1. Most of these methods are derived for the 2D (tomographic) case and are being adapted to the allow for 3D reconstruction.

Among the earliest is the layer stripping method [119, 66], with an another example being the D-bar ($\bar{\partial}$) algorithms [78, 76, 77], which were tested on tank phantoms [98] and on human chest data [40, 64] in the 2D case. Furthermore, the D-bar method was extended to the third dimension by Bikowski et. al. [16].

Most of the regularization strategies mentioned rely on adding a penalty term to the least squares problem usually imposing a constraint on the 'size' of the solution (i.e in terms of smoothness). The inclusion of this term is controlled by a real number usually denoted λ throughout this chapter - the *regularization parameter*. Finding a suitable value of this parameter represents an another problem to be considered. There are a number of strategies for determining its appropriate value for given data such as L-curve analysis [56]. Unfortunately, ideas behind these methods are outside the scope of this thesis.

5. The EIDORS Software Package

This chapter gives some examples of using the Electrical Impedance and Diffuse Optical Reconstruction Software (EIDORS) to manipulate EIT data and to perform both forward and inverse calculations. For an introduction to the ideas behind the software solution and its history see section 1.4.

There are a number of published works describing some of the software internals written in Matlab [9, 10, 107, 108] and an internet page dedicated to the package is maintained by its developers providing tutorials and Matlab function documentation [1]. However, a comprehensive reference manual detailing the implementation is missing.

In the following sections, a basic overview of EIDORS functionality will be given and examples of both forward and inverse calculations will be presented.

5.1 EIDORS structures and functionality

EIDORS operates as a Matlab module with four types of structures - **fwd_model**, **inv_model**, **data**, **image**. Representing all the essential stages of solving the EIT problem from data representation to visualization of results.

The **fwd_model** structure contains data specifying the geometry of a finite element mesh modeling the domain of interest along with electrode data (corresponding faces of boundary elements and contact impedances), stimulation and measurement patterns and function pointers representing the choices of forward solver functions for performing the forward computation and for the construction of the Jacobian (a linearization of the forward operator) utilized by Gauss-Newton inverse solvers.

The **inv_model** structure contains the geometry of the mesh we want to utilize for the inverse calculation (often a coarser mesh is chosen for the inverse calculation), function pointers to desired inverse solvers and regularization strategies, a choice of a regularization parameter (termed 'hyperparameter' in EIDORS). An inverse model may be constructed explicitly from a forward model assuming the same geometry.

The **data** structure represents all the measurements the system took according to the prescribed stimulation pattern and is used by inverse solvers to perform image reconstruction.

The **image** structure is constructed from a forward model and carries data about the conductivity/admittivity distribution within the domain - which is represented by a piecewise constant function on the finite elements of the model. The image structure is handled by a plethora of EIDORS visualization functions which are used to display the domain conductivity layout for the forward model (if we choose to map some of its structures we are confident about) and the results of inverse computations. Examples of such functions are **show_fem** and **show_slices** (the former displays the conductivity distribution within the 2D/3D FEM geometry while the latter computes the distribution within set of slices through the 3D object specified by the user).

5.2 Examples of use

This section presents a number of simulations of the forward and inverse calculation performed in both two and three dimensions. For the purpose of examining the functionality of EIDORS, matlab scripts listed in table 5.1 were written by the author of this thesis and will be made available for download to the readers. All of the graphical outputs of the scripts will be presented in this chapter. Furthermore, being relatively simple, the code of two scripts for the 2D case will be listed in this thesis for illustrative purposes.

Table 5.1: A list of Matlab scripts written to explore EIDORS functionalities

`forward_2D()`	Forward calculation for a disc domain in two dimensions with the visualization of the first current patern of an adjacent stimulation protocol
`/thesis_examples/img/forward_2D/`	
`inverse_2D()`	Inverse calculation for a disc domain in two dimensions with noise-free data and the visualization of results
`/thesis_examples/img/inverse_2D/`	
`inverse_2D_noise(snr,hyperparam)`	Inverse calculation for a disc domain in two dimensions with noise-contaminated data called with snr - signal-to-noise ratio and hyperparam - regularization parameter for the Tikhonov regularization strategy
`/thesis_examples/img/inverse_2D/`	
`forward_3D()`	Forward calculation for a hemispherical domain in three dimensions with the visualization of the first current patern of a ring-wise adjacent stimulation pattern
`/thesis_examples/img/forward_3D/`	
`inverse_3D()`	Inverse calculation from noise-free data for a hemispherical domain with a spherical inclusion in three dimensions with the visualization of results
`/thesis_examples/img/forward_3D/clean/`	
`inverse_3D_noise(snr,hyperparam)`	Inverse calculation from noise-contaminated data for a hemispherical domain with a spherical inclusion in three dimensions with visualization accepting two arguments having the same purpose as in the 2D case
`/thesis_examples/img/forward_3D/noise/`	

5.2.1 Forward modelling and calculations

In two dimensions, calculations are preformed in a disc domain whose forward model is constructed by a built-in common model assembly function **mk_common_model** accepting a control string specifying the geometry and refinement of the domain mesh. Similarly, stimulation and measurement patterns are assembled by a built-in function and thus it is easy to specify common pair drive patterns such as the adjacent drive chosen for the 2D examples.

While common 3D models are also accessible via built-in EIDORS functions, the true power of the 3D reconstruction software lies in the ability to work with an arbitrary geometry of the domain when its mesh parameters are passed to the software. Positions of nodes and their connectivity along with the selection of boundary elements may be generated by any software and used by EIDORS via manual specification based on the output of the given mesh software. However, EIDORS was integrated with Netgen meshing software [113] and offers forward model constructors directly accepting Constructive Solid Geometry (CSG) input for Netgen. For the 3D simulations a hemispherical domain with radius $r = 80$ mm was chosen.

Furthermore, integration with Netgen allows the user to specify electrode positions on the domain boundary and their geometry (the constructor accepts Cartesian coordinates of electrodes, corresponding unit normals to the boundary and specifications of shapes to be projected onto the boundary at these coordinates). In the examples package, electrode positions and unit normals are generated by the **get_electrode_positions()** function. In the 3D examples, a total of 64 electrodes was divided into eight rings forming regular octagons in horizontal slices through the hemisphere equally spaced in the z coordinate.

Once the positions of electrodes are determined, stimulation patterns may be assigned to the forward model and need to be assembled manually for user-specified models. For the purpose of the 3D simulations, this is handled by the function **get_stim_patterns()**. Current patterns were chosen so as to apply the adjacent protocol on each ring totaling 64 stimulations, while measurements are also taken as differences between adjacent electrodes in a ring for each stimulation pattern giving a total of 4096 measurements.

The visualizations of electric potential distribution within the domains for the first current pattern in both the 2D and 3D case are shown in figures 5.1, 5.6.

5.2.2 Inverse calculations

There are two scripts for inverse calculations for each dimension. In all four cases, the inverse calculation is performed by a Gauss-Newton one step difference solver. The inverse solver therefore accepts two sets of data, one representing 'earlier' measurements taken for a homogenous conductivity distribution and the second containing measurements with the inclusion. This algorithm then performs one step of the Gauss-Newton method based on linearising the forward operator around the earlier conductivity. All four scripts rely on the standard Tikhonov Regularization strategy.

In the 2D case a ten times more conductive disc inclusion was introduced into the domain of homogenous conductivity of 0.1 S/m seen in figure 5.2, while in the

3D case a spherical inclusion having 0.2 S/m conductivity was introduced into a homogenous distribution of 0.1 S/m as depicted by figure 5.7.

The inverse problem examples further split based on whether we are taking noise in the data into account. The **inverse_2D_noise** and **inverse_3D_noise** scripts need to be supplied with two parameters **snr** and **hyperparam**. The **snr** argument specifies how high is the simulated system SNR.

The base noise amplitude is taken to be the standard deviation of the difference between the corresponding homogenous and inhomogenous conductivity distribution measurements (component-wise). The data vector is then contaminated by a random vector amplified by the computed noise factor.

The second parameter **hyperparam** is the 'hyperparameter' representing a regularization parameter controlling the influence of the respective penalty term introduced into the least-squares problem based on a chosen regularization strategy. When the Tikhonov regularization strategy is chosen, the penalty term gives preference to solutions with smaller norms and effectively controls the amount of noise introduced into the problem. The regularization parameter needs to be selected appropriately for a given strategy and noise level. There are a number of strategies for selecting a hyperparameter value based on analyzing the data set and tweaking these parameters so as to achieve higher quality of images should be avoided in EIT practice because in a practical situation, we do not know what is actually inside the domain. This is however outside the scope of this thesis and the examples in this chapter require the user to select the hyperparameter manually. The influence of hyperparameter selection may be seen in images 5.3, 5.4, 5.5 showing an underregularized solution, a solution corresponding to an appropriate choice of hyperparameter and an overregularized solution. In an underregularized solution, the influence of noise was not suppressed enough by the regularization technique and the noise takes over the solution. An overregularized solution has been stripped of useful components to a certain degree meaning a part of information was washed out in the process of regularization.

The result of a conductivity distribution reconstruction is shown in figure 5.4 representing the 2D case and in figures 5.8, 5.9 in the 3D case.

Listing 5.1: forward_2D() - the forward calculation in 2D

```
%Start EIDORS
startup;

%Create a model using EIDORS built-in common model assembly
%command - circular model with 16 electrodes, 1024 elements
test_model = mk_common_model('d2C',16);

%Display mesh
% figure;
% show_fem(test_model.fwd_model);

%Create an EIDORS image structure
test_img = mk_image(test_model);

%Create an adjacent stimulation pattern using a command for common
%model stimulation patterns - 16 electrodes, 1 electrode ring,
%adjacent drive, adjacent measurement, no options,
%10 mA current amplitude
[stim,meas_sel] = mk_stim_patterns(16,1,'{ad}','{ad}',{},0.01);
```

```
20
21 %Assign patterns to image structure
22 test_img.fwd_model.stimulation = stim;
23 test_img.fwd_model.meas_select = meas_sel;
24
25 %Collect potential at all nodes
26 test_img.fwd_solve.get_all_meas = 1;
27
28 %Perform the forward calculation using default A.Adler solver
29 hom_data = fwd_solve(test_img);
30
31 %Display first stimulation pattern
32 display_img = rmfield(test_img, 'elem_data');
33 display_img.node_data = hom_data.volt(:,1);
34 figure();
35 show_fem(display_img);
36 end
```

Listing 5.2: inverse_2D_noise(snr,hyperparam) - the 2D inverse computation with noise-contaminated measurements

```
1  function inverse_2d_noise(snr,hyperparam)
2  %Start EIDORS
3  startup;
4
5  %Create a model using EIDORS built-in common model assembly command
6  %Circular model with 16 electrodes, 1024 elements, plus a finer mesh
7  % of 4096 elements
8  coarse_model = mk_common_model('d2C',16);
9  fine_model = mk_common_model('h2C',16);
10
11 %Create an EIDORS image structure representing a homogenous
12 %conductivity distribution of 0.1 S/m
13 fine_img = mk_image(fine_model,0.1);
14
15 %Create an adjacent stimulation pattern using a command for common
16 % model stimulation patterns - 16 electrodes, 1 electrode ring,
17 %adjacent drive, adjacent measurement, no options,
18 %10 mA current amplitude
19 [stim,meas_sel] = mk_stim_patterns(16,1,'{ad}','{ad}',{},0.01);
20
21 %Assign patterns to image structure
22 fine_img.fwd_model.stimulation = stim;
23 fine_img.fwd_model.meas_select = meas_sel;
24
25 %Perform the forward calculation using default A.Adler  solver
26 hom_data = fwd_solve(fine_img);
27
28 %Introduce a 10 times more conductive cirucular inhomogeneity
29 %into the domain and perform the forward calculation
30 shape_1 = @(x,y,z) ((x-0.5).^2 + (y-0.2).^2 < 0.15^2);
31 fine_img.elem_data = fine_img.elem_data + 0.9*elem_select(...
32     fine_model.fwd_model,shape_1);
33
34 figure();
35 show_fem(fine_img);
36
37 inh_data = fwd_solve(fine_img);
```

```
38
39 %Contaminate data with noise, SNR = 20*log_10(A_signal/A_noise)
40 inh_data_noise = inh_data;
41 nampl = std(hom_data.meas - inh_data.meas)*10^(-snr/20);
42 inh_data_noise.meas = inh_data.meas + ...
43         nampl*randn(size(inh_data.meas));
44
45 %Create an inverse model object - difference imaging
46 inv_model = eidors_obj('inv_model', 'EIT_inverse');
47 inv_model.reconst_type = 'difference';
48 inv_model.jacobian_bkgnd.value = 0.1;
49 inv_model.fwd_model = coarse_model.fwd_model;
50
51 %Use a Gauss-Newton solver performing one step difference
52 %reconstruction on a coarser mesh
53 inv_model.solve = @inv_solve_diff_GN_one_step;
54
55 %Choose the Tikhonov (L = parameter*identity matrix)
56 %regularization strategy
57
58 inv_model.hyperparameter.value = hyperparam;
59 inv_model.RtR_prior = @prior_tikhonov;
60
61 %Perform the inverse calculation and display the result
62 rec_image = inv_solve(inv_model, hom_data, inh_data_noise);
63 figure();
64 show_fem(rec_image);
65 end
```

Figure 5.1: forward_2D - First stimulation pattern of an adjacent drive

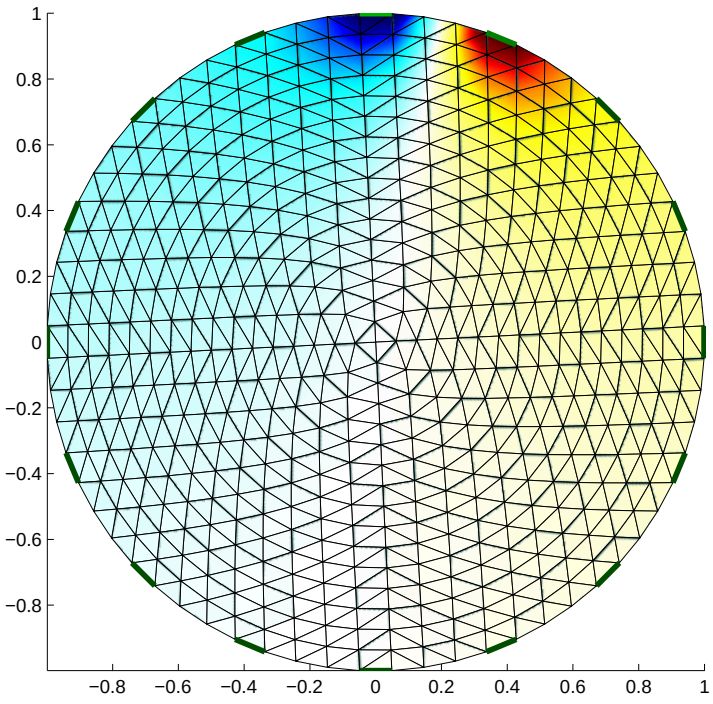

Figure 5.2: inverse_2D_noise - The disc inclusion

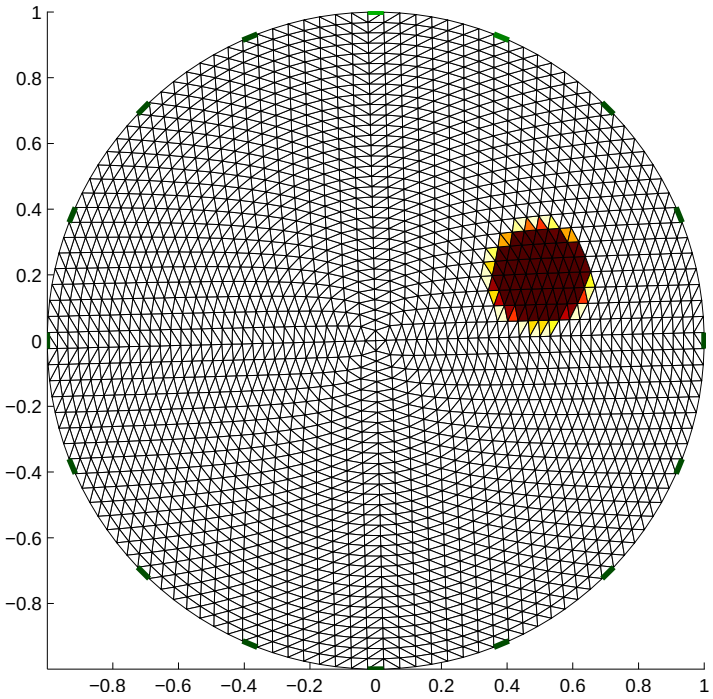

Figure 5.3: inverse_2D_noise - Reconstructed distribution from 12 dB SNR data with hyperparameter $\lambda = 10^{-3}$. The solution is overwhelmed by noise.

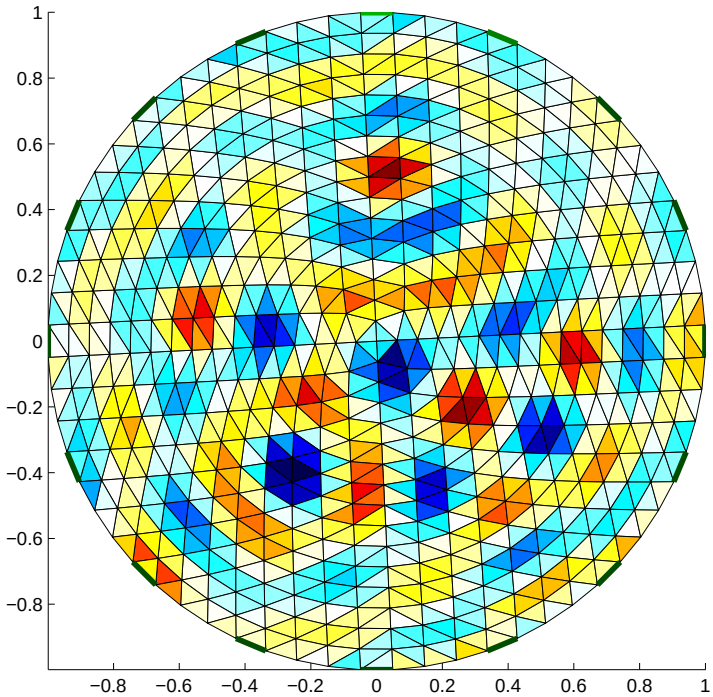

Figure 5.4: inverse_2D_noise - Reconstructed distribution from 12 dB SNR data with hyperparameter $\lambda = 1$. The hyperparameter is appropriate for the level of noise in data.

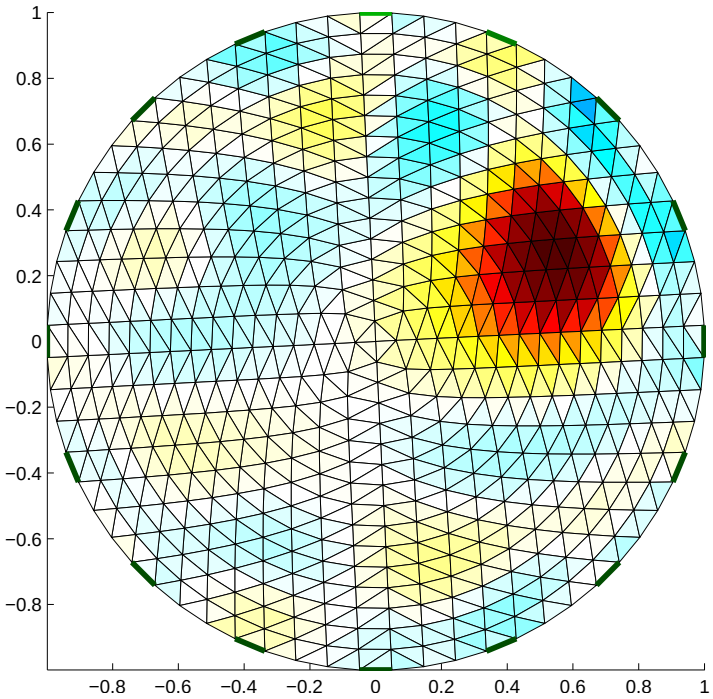

Figure 5.5: inverse_2D_noise - Reconstructed distribution from 12 dB SNR data with hyperparameter $\lambda = 10^2$. The solution is overregularized with its useful components dampened.

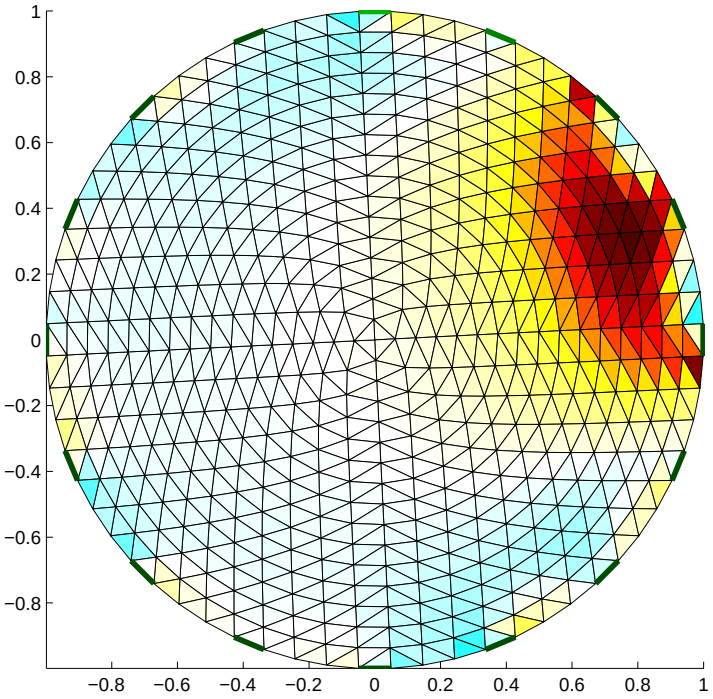

Figure 5.6: forward_3D - First stimulation pattern of the ring-wise adjacent stimulation protocol

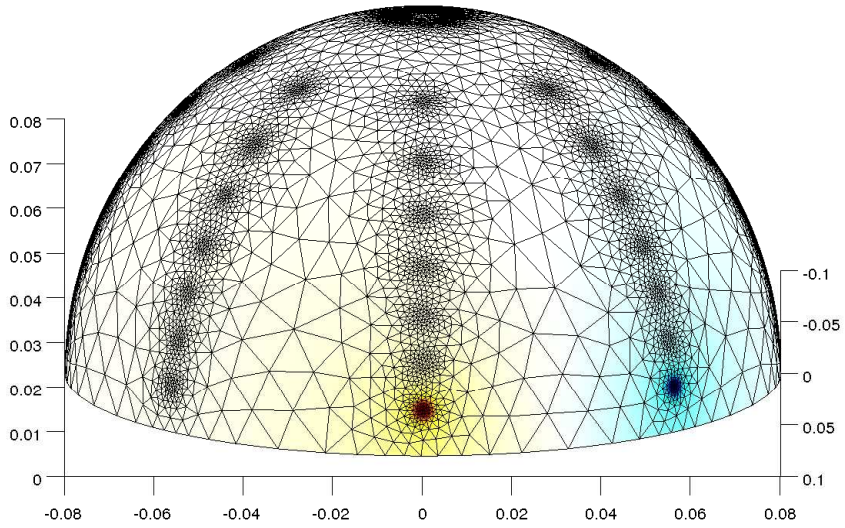

Figure 5.7: inverse_3D_noise - The spherical inclusion

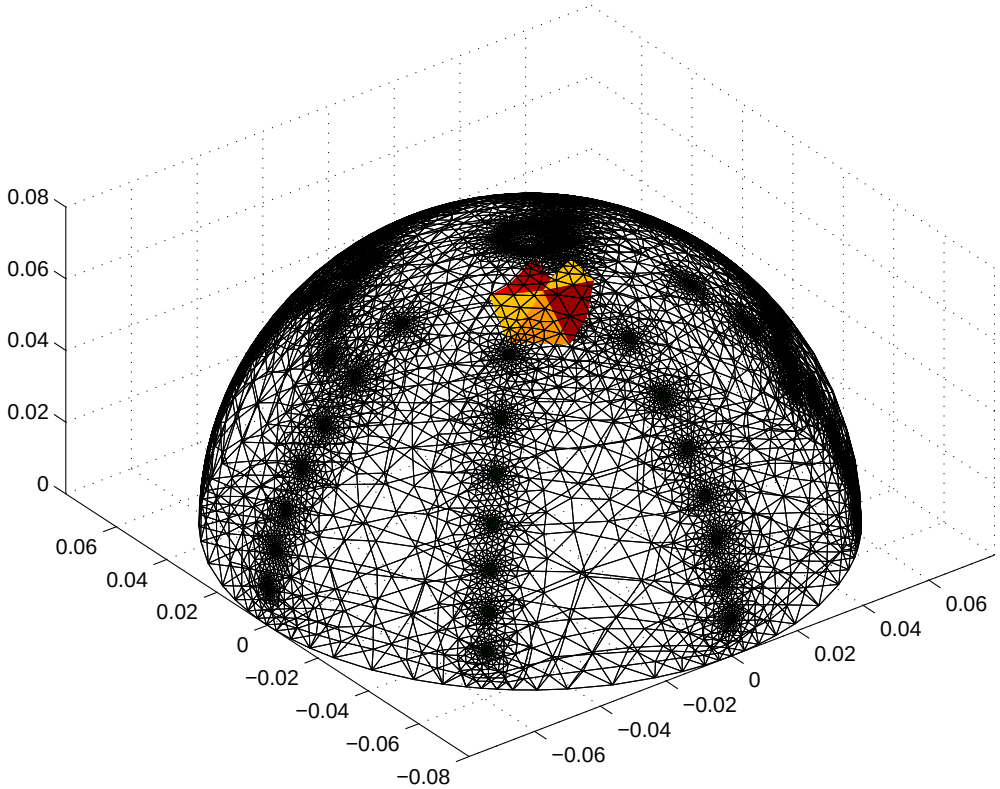

Figure 5.8: inverse_3D_noise - Reconstructed distribution from 12 dB SNR data with hyperparameter $\lambda = 10^{-3}$

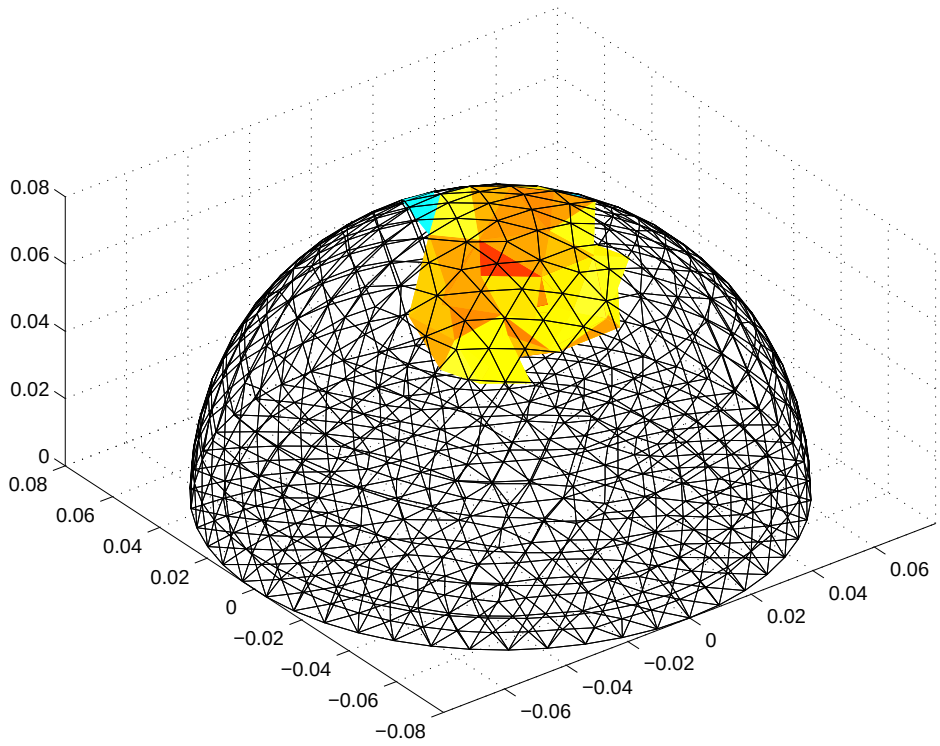

Figure 5.9: Horizontal slices through the hemisphere at $z = 0.030$, 0.040, 0.050, 0.060

(a) The original inclusion

(b) Reconstructed distribution from 12 dB SNR data with hyperparameter $\lambda = 10^{-3}$

Conclusion

Out of all the areas, where Electrical Impedance Tomography (EIT) shows potential as an imaging technique, medical applications, namely breast cancer detection, were investigated. In order to form a qualitative picture of the response of biological tissue to electrical currents and its frequency dependence a literature review was conducted. The reviewed data indicate, that while magnetic induction in tissue may be neglected, its capacitive properties can not be omitted. Furthermore, the rationale behind using EIT as an imaging technique for breast cancer detection was examined. Researchers agree, that there is a significant difference between the dielectrical properties of healthy and cancerous breast tissue, the magnitude of which depends on frequency. These claims are supported by the clinical success of a number of EIT devices constructed to date for the purpose of breast cancer detection with a total of eight systems described in this thesis. It was demonstrated that, the earlier Electrical Impedance Mapping (EIM) systems can compete with established breast imaging techniques such as mammography.

Reconstruction of a conductivity distribution within a physical body from voltage measurements (the inverse problem) acquired on its boundary poses many challenges. It can be classified as an inverse boundary value problem and thus falls into a common framework of inverse problem theory. First of all, many EIT image reconstruction algorithms require the calculation of the potential distribution within the body in order to match the corresponding boundary data with the actual measurements (the forward problem). For this purpose, the governing equations of the EIT problem were derived and the means of solving them numerically via the Finite Element Method were described.

Means of solving the EIT inverse problem in three dimensions numerically were described. As the problem inherently suffers from a shortage of information, attempts to solve it numerically lead to ill-conditioned systems of equations. This has to be remedied i.e. by the means of regularization. Regularization techniques and means of introducing them into the formulation of the EIT inverse problem were described.

In the last chapter, the capabilities of the Electrical Impedance and Diffuse Optical Reconstruction Software (EIDORS) package were examined. Examples of forward and inverse calculations in both 2D and 3D are available via six Matlab scripts with the corresponding graphical output included in the chapter.

In summary, it can be concluded, that EIT shows potential as an imaging modality not only in medical practice. However, there are a number of optimization problems that need to be tackled in order to improve the quality of images produced by the technique such as reduction of noise in the system circuitry, choosing an advantageous placement of electrodes for a given application and electrical current stimulation pattern selection. There is also room for improvement in the area of reconstruction algorithms, namely for the development of fully nonlinear approaches to the inverse problem. Another issue to be addressed is the fragmentation of the EIT knowledge base. To ensure the effectivity of EIT research, a unified source of information about the technique should be maintained by active researchers.

Bibliography

[1] EIDORS function documentation. `http://eidors3d.sourceforge.net/`. Accessed: 2015-04-05.

[2] EIDORS function documentation - index for eidors/solvers/forward. `http://eidors3d.sourceforge.net/doc/eidors/solvers/forward/menu.html`. Accessed: 2015-04-04.

[3] MathWorks - Matlab Documentation. `http://www.mathworks.com/help/matlab/index.html`. Accessed: 2015-04-05.

[4] OOO PKF 'SIM-technika' - Products : History of the device creation. `http://www.impedance.ru/en/product_hist.html`. Accessed: 2015-03-13.

[5] Juan-Felipe PJ Abascal, Simon R Arridge, David Atkinson, Raya Horesh, Lorenzo Fabrizi, Marzia De Lucia, Lior Horesh, Richard H Bayford, and David S Holder. Use of anisotropic modelling in electrical impedance tomography; description of method and preliminary assessment of utility in imaging brain function in the adult human head. *Neuroimage*, 43(2):258–268, 2008.

[6] Andy Adler, Marcelo B Amato, John H Arnold, Richard Bayford, Marc Bodenstein, Stephan H Böhm, Brian H Brown, Inéz Frerichs, Ola Stenqvist, Norbert Weiler, et al. Whither lung EIT: Where are we, where do we want to go and what do we need to get there? *Physiological measurement*, 33(5):679, 2012.

[7] Andy Adler, John H Arnold, Richard Bayford, Andrea Borsic, Brian Brown, Paul Dixon, Theo JC Faes, Inéz Frerichs, Hervé Gagnon, Yvo Gärber, et al. GREIT: a unified approach to 2D linear EIT reconstruction of lung images. *Physiological measurement*, 30(6):S35, 2009.

[8] Andy Adler, Pascal Olivier Gaggero, and Yasheng Maimaitijiang. Adjacent stimulation and measurement patterns considered harmful. *Physiological measurement*, 32(7):731, 2011.

[9] Andy Adler and William RB Lionheart. EIDORS: Towards a community-based extensible software base for EIT. In *6th Conference on Biomedical Applications of Electrical Impedance Tomography, London, UK*, pages 1–4, 2005.

[10] Andy Adler and William RB Lionheart. Uses and abuses of EIDORS: an extensible software base for EIT. *Physiological measurement*, 27(5):S25, 2006.

[11] Michel Assenheimer, Orah Laver-Moskovitz, Dov Malonek, David Manor, Udi Nahaliel, Ron Nitzan, and Abraham Saad. The T-SCAN ™technology: electrical impedance as a diagnostic tool for breast cancer detection. *Physiological Measurement*, 22(1):1, 2001.

[12] NJ Avis and DC Barber. Image reconstruction using non-adjacent drive configurations (electric impedance tomography). *Physiological measurement*, 15(2A):A153, 1994.

[13] DC Barber and BH Brown. Applied potential tomography. *Journal of physics. E. Scientific instruments*, 17(9):723–733, 1984.

[14] DC Barber, BH Brown, and IL Freeston. Imaging spatial distributions of resistivity using applied potential tomography. In *Information Processing in Medical Imaging*, pages 446–462. Springer, 1984.

[15] RH Bayford. Bioimpedance tomography (electrical impedance tomography). *Annu. Rev. Biomed. Eng.*, 8:63–91, 2006.

[16] Jutta Bikowski, Kim Knudsen, and Jennifer L Mueller. Direct numerical reconstruction of conductivities in three dimensions using scattering transforms. *Inverse Problems*, 27(1):015002, 2011.

[17] Börje Blad and Bo Baldetorp. Impedance spectra of tumour tissue in comparison with normal tissue; a possible clinical application for electrical impedance tomography. *Physiological Measurement*, 17(4A):A105, 1996.

[18] BH Blott, GJ Daniell, and S Meeson. Electrical impedance tomography with compensation for electrode positioning variations. *Physics in medicine and biology*, 43(6):1731, 1998.

[19] KG Boone and DS Holder. Current approaches to analogue instrumentation design in electrical impedance tomography. *Physiological measurement*, 17(4):229, 1996.

[20] Andrea Borsic. *Regularisation methods for imaging from electrical measurements*. PhD thesis, Oxford Brookes University, 2002.

[21] Andrea Borsic, Brad M Graham, Andy Adler, and W Lionheart. In vivo impedance imaging with total variation regularization. *Medical Imaging, IEEE Transactions on*, 29(1):44–54, 2010.

[22] Andrea Borsic, William RB Lionheart, and Christoher N. McLeod. Generation of anisotropic-smoothness regularization filters for EIT. *Medical Imaging, IEEE Transactions on*, 21(6):579–587, 2002.

[23] William Robert Breckon. *Image reconstruction in electrical impedance tomography*. PhD thesis, Oxford Polytechnic, 1990.

[24] David J Brenner and Eric J Hall. Computed tomography, an increasing source of radiation exposure. *New England Journal of Medicine*, 357(22):2277–2284, 2007.

[25] Susanne C Brenner and Ridgway Scott. *The mathematical theory of finite element methods*, volume 15. Springer Science & Business Media, 2008.

[26] BH Brown and AD Seagar. The Sheffield data collection system. *Clinical Physics and Physiological Measurement*, 8(4A):91, 1987.

[27] Mark A Brown and Richard C Semelka. *MRI: basic principles and applications*. John Wiley & Sons, 2011.

[28] R Phillip Burns. Image-guided breast biopsy. *The American journal of surgery*, 173(1):9–11, 1997.

[29] Alberto P. Calderón. On an inverse boundary value problem. *Comp. Appl. Math*, 25(2-3), 2006. REPRINT.

[30] Jan Campbell and Nicola Dimache. 3D EIT - MEIK in clinical application: observations and preliminary results. In *World Congress on Medical Physics and Biomedical Engineering 2006*, pages 3906–3910. Springer, 2007.

[31] M Cheney, D Isaacson, JC Newell, S Simske, and J Goble. NOSER: An algorithm for solving the inverse conductivity problem. *International Journal of Imaging Systems and Technology*, 2(2):66–75, 1990.

[32] Margaret Cheney and David Isaacson. Distinguishability in impedance imaging. *Biomedical Engineering, IEEE Transactions on*, 39(8):852–860, 1992.

[33] Margaret Cheney, David Isaacson, and Jonathan C Newell. Electrical impedance tomography. *SIAM review*, 41(1):85–101, 1999.

[34] Kuo-Sheng Cheng, David Isaacson, JC Newell, and David G Gisser. Electrode models for electric current computed tomography. *Biomedical Engineering, IEEE Transactions on*, 36(9):918–924, 1989.

[35] Vladimir Cherepenin, A Karpov, A Korjenevsky, V Kornienko, A Mazaletskaya, D Mazourov, and D Meister. A 3D electrical impedance tomography (EIT) system for breast cancer detection. *Physiological measurement*, 22(1):9, 2001.

[36] Vladimir A Cherepenin, Alexander Y Karpov, Alexander V Korjenevsky, Valdimir N. Kornienko, Yury S Kultiasov, Mikhail B Ochapkin, Olga V Trochanova, and J David Meister. Three-dimensional EIT imaging of breast tissues: system design and clinical testing. *Medical Imaging, IEEE Transactions on*, 21(6):662–667, 2002.

[37] Myoung Hwan Choi, Tzu-Jen Kao, David Isaacson, GJASGJ Saulnier, and Jonathan C Newell. A reconstruction algorithm for breast cancer imaging with electrical impedance tomography in mammography geometry. *Biomedical Engineering, IEEE Transactions on*, 54(4):700–710, 2007.

[38] Raymond D Cook, G Saulnier, David G Gisser, John C Goble, JC Newell, and David Isaacson. ACT3: A high-speed, high-precision electrical impedance tomograph. *Biomedical Engineering, IEEE Transactions on*, 41(8):713–722, 1994.

[39] J Estrela Da Silva, JP Marques de Sá, and J Jossinet. Classification of breast tissue by electrical impedance spectroscopy. *Medical and Biological Engineering and Computing*, 38(1):26–30, 2000.

[40] M DeAngelo and JL Mueller. 2D D-bar reconstructions of human chest and tank data using an improved approximation to the scattering transform. *Physiological measurement*, 31(2):221, 2010.

[41] Hamid Dehghani and Manuchehr Soleimani. Numerical modelling errors in electrical impedance tomography. *Physiological measurement*, 28(7):S45, 2007.

[42] Lawrence Evans. *Partial differential equations*. American Mathematical Society, 1998.

[43] Stephen A Feig and R Edward Hendrick. Radiation risk from screening mammography of women aged 40-49 years. *JNCI Monographs*, 1997(22):119–124, 1997.

[44] J Forsyth, A Borsic, RJ Halter, A Hartov, and KD Paulsen. Optical breast shape capture and finite-element mesh generation for electrical impedance tomography. *Physiological measurement*, 32(7):797, 2011.

[45] Hugo Fricke and Sterne Morse. The electric capacity of tumors of the breast. *The Journal of Cancer Research*, 10(3):340–376, 1926.

[46] Camelia Gabriel. Compilation of the dielectric properties of body tissues at rf and microwave frequencies. Technical report, DTIC Document, 1996.

[47] Camelia Gabriel, Sami Gabriel, and E Corthout. The dielectric properties of biological tissues: I. literature survey. *Physics in medicine and biology*, 41(11):2231, 1996.

[48] S Gabriel, RW Lau, and Camelia Gabriel. The dielectric properties of biological tissues: II. Measurements in the frequency range 10 Hz to 20 GHz. *Physics in medicine and biology*, 41(11):2251, 1996.

[49] Sami Gabriel, RW Lau, and Camelia Gabriel. The dielectric properties of biological tissues: III. Parametric models for the dielectric spectrum of tissues. *Physics in medicine and biology*, 41(11):2271, 1996.

[50] Henrik Garde. *Sparsity Regularization for Electrical Impedance Tomography*. PhD thesis, Technical University of Denmark, 2013.

[51] Yael A. Glickman, Orna Filo, Udi Nachaliel, Sarah Lenington, Sigal Amin-Spector, and Ron Ginor. Novel EIS postprocessing algorithm for breast cancer diagnosis. *Medical Imaging, IEEE Transactions on*, 21(6):710–712, 2002.

[52] Gene H Golub and Charles F Van Loan. *Matrix Computations*, volume 3. JHU Press, 2013.

[53] Peter C Gøtzsche and Margrethe Nielsen. Screening for breast cancer with mammography. *The cochrane library*, 2009.

[54] R Halter, A Hartov, S Poplack, R diFlorio Alexander, W Wells, K Rosenkranz, R Barth, P Kaufman, and K Paulsen. Real-time electrical impedance variations in women with and without breast cancer. 2015.

[55] Ryan J Halter, Alex Hartov, and Keith D Paulsen. A broadband high-frequency electrical impedance tomography system for breast imaging. *Biomedical Engineering, IEEE Transactions on*, 55(2):650–659, 2008.

[56] Per Christian Hansen. *Rank-deficient and discrete ill-posed problems: numerical aspects of linear inversion*, volume 4. Siam, 1998.

[57] A. Hartov, R.A. Mazzarese, F.R. Reiss, T.E. Kerner, K.S. Osterman, D.B. Williams, and K.D. Paulsen. A multichannel continuously selectable multi-frequency electrical impedance spectroscopy measurement system. *Biomedical Engineering, IEEE Transactions on*, 47(1):49–58, Jan 2000.

[58] Ahmed M Hassan and Magda El-Shenawee. Review of electromagnetic techniques for breast cancer detection. *Biomedical Engineering, IEEE Reviews in*, 4:103–118, 2011.

[59] Ross P Henderson and John G Webster. An impedance camera for spatially specific measurements of the thorax. *Biomedical Engineering, IEEE Transactions on*, (3):250–254, 1978.

[60] Gabor T Herman. *Fundamentals of computerized tomography: image reconstruction from projections*. Springer Science & Business Media, 2009.

[61] David S Holder. *Electrical impedance tomography: methods, history and applications*. CRC Press, 2004.

[62] Umer Zeeshan Ijaz, Bong Seok Kim, Tzu-Jen Kao, Anil Kumar Khambampati, Sin Kim, Min Chan Kim, Jonathan C Newell, David Isaacson, and Kyung Youn Kim. Mammography phantom studies using 3D electrical impedance tomography with numerical forward solver. In *Frontiers in the Convergence of Bioscience and Information Technologies, 2007. FBIT 2007*, pages 379–383. IEEE, 2007.

[63] Oleg Imanuvilov, Gunther Uhlmann, and Masahiro Yamamoto. The calderón problem with partial data in two dimensions. *Journal of the American Mathematical Society*, 23(3):655–691, 2010.

[64] D Isaacson, JL Mueller, JC Newell, and S Siltanen. Imaging cardiac activity by the D-bar method for electrical impedance tomography. *Physiological measurement*, 27(5):S43, 2006.

[65] David Isaacson. Distinguishability of conductivities by electric current computed tomography. *Medical Imaging, IEEE Transactions on*, 5(2):91–95, 1986.

[66] Sylvester John. A convergent layer stripping algorithm for the radially symmetric impedence tomography problem. *Communications in partial differential equations*, 17(11-12):1955–1994, 1992.

[67] J Jossinet. Variability of impedivity in normal and pathological breast tissue. *Medical and Biological Engineering and Computing*, 34(5):346–350, 1996.

[68] J Jossinet, C Fourcade, and M Schmitt. A study for breast imaging with a circular array of impedance electrodes. In *Proc. Vth Int. Conf. Bioelectrical Impedance*, pages 83–86, 1981.

[69] J Jossinet, A Lobel, C Michoudet, and M Schmitt. Quantitative technique for bio-electrical spectroscopy. *Journal of biomedical engineering*, 7(4):289–294, 1985.

[70] Jacques Jossinet. The impedivity of freshly excised human breast tissue. *Physiological measurement*, 19(1):61, 1998.

[71] Jari P Kaipio, Ville Kolehmainen, Erkki Somersalo, and Marko Vauhkonen. Statistical inversion and Monte Carlo sampling methods in electrical impedance tomography. *Inverse problems*, 16(5):1487, 2000.

[72] Tzu-Jen Kao, Gary J Saulnier, Hongjun Xia, Chandana Tamma, JC Newell, and D Isaacson. A compensated radiolucent electrode array for combined EIT and mammography. *Physiological measurement*, 28(7):S291, 2007.

[73] Carlos E Kenig, Johannes Sjöstrand, and Gunther Uhlmann. The calderón problem with partial data. *Annals of mathematics*, pages 567–591, 2007.

[74] Todd E Kerner, Keith D Paulsen, Alex Hartov, Sandra K Soho, and Steven P Poplack. Electrical impedance spectroscopy of the breast: clinical imaging results in 26 subjects. *Medical Imaging, IEEE Transactions on*, 21(6):638–645, 2002.

[75] Klaus Knödel, Gerhard Lange, and Hans-Jürgen Voigt. *Environmental geology: handbook of field methods and case studies*. Springer Science & Business Media, 2007.

[76] Kim Knudsen, Matti Lassas, Jennifer L Mueller, and Samuli Siltanen. D-bar method for electrical impedance tomography with discontinuous conductivities. *SIAM Journal on Applied Mathematics*, 67(3):893–913, 2007.

[77] Kim Knudsen, Matti Lassas, Jennifer L Mueller, and Samuli Siltanen. Regularized D-bar method for the inverse conductivity problem. *Inverse Problems and Imaging*, 35(4):599, 2009.

[78] Kim Knudsen and Alexandru Tamasan. Reconstruction of less regular conductivities in the plane. *Communications in Partial Differential Equations*, 1:28, 2003.

[79] DM Koh and AR Padhani. *Diffusion-weighted MRI: a new functional clinical technique for tumour imaging*. British Institute of Radiology, 2014.

[80] V Kolehmainen, M Vauhkonen, PA Karjalainen, and JP Kaipio. Assessment of errors in static electrical impedance tomography with adjacent and trigonometric current patterns. *Physiological measurement*, 18(4):289, 1997.

[81] GL Lamont, JW Wright, DF Evans, and L Kapila. An evaluation of applied potential tomography in the diagnosis of infantile hypertrophic pyloric stenosis. *Clinical Physics and Physiological Measurement*, 9(4A):65, 1988.

[82] Paul C Lauterbur et al. Image formation by induced local interactions: examples employing nuclear magnetic resonance. *Nature*, 242(5394):190–191, 1973.

[83] Kim Hwa Lim, Joon-Ho Lee, Gang Ye, and Qing Huo Liu. An efficient forward solver in electrical impedance tomography by spectral element method. *Medical Imaging, IEEE Transactions on*, 25(8):1044–1051, 2006.

[84] William RB Lionheart. EIT reconstruction algorithms: pitfalls, challenges and recent developments. *Physiological Measurement*, 25(1):125, 2004.

[85] WRB Lionheart, SR Arridge, M Schweiger, M Vauhkonen, and JP Kaipio. Electrical impedance and diffuse optical tomography reconstruction software. In *Proceedings of 1st World Congress on Industrial Process Tomography*, pages 474–477, 1999.

[86] Dong Liu, Ville Kolehmainen, Samuli Siltanen, and Aku Seppänen. A nonlinear approach to difference imaging in EIT; assessment of the robustness in the presence of modelling errors. *Inverse Problems*, 31(3):035012, 2015.

[87] Ning Liu. *ACT4: A high-precision, multi-frequency electrical impedance tomograph*. ProQuest, 2007.

[88] MH Loke. Electrical imaging surveys for environmental and engineering studies. *A practical guide to*, 2, 1999.

[89] PK Manwaring, RJ Halter, A Borsic, and A Hartov. A modified electrode configuration for brain EIT. In *Journal of Physics: Conference Series*, volume 224, page 012062. IOP Publishing, 2010.

[90] Preston Manwaring, Ryan Halter, Yuqing Wan, Andrea Borsic, Alex Hartov, and Keith Paulsen. Arbitrary geometry patient interfaces for breast cancer detection and monitoring with electrical impedance tomography. In *Engineering in Medicine and Biology Society, 2008. EMBS 2008. 30th Annual International Conference of the IEEE*, pages 1178–1180. IEEE, 2008.

[91] Donald W Marquardt. An algorithm for least-squares estimation of nonlinear parameters. *Journal of the Society for Industrial & Applied Mathematics*, 11(2):431–441, 1963.

[92] Gonzalo Martín, Rocío Martín, María Brieva, and Luis Santamaría. Electrical impedance scanning in breast cancer imaging: correlation with mammographic and histologic diagnosis. *European radiology*, 12(6):1471–1478, 2002.

[93] A McEwan, A Romsauerova, R Yerworth, Lior Horesh, Richard Bayford, and D Holder. Design and calibration of a compact multi-frequency EIT system for acute stroke imaging. *Physiological measurement*, 27(5):S199, 2006.

[94] Marc Molinari, Barry H Blott, Simon J Cox, and Geoffrey J Daniell. Optimal imaging with adaptive mesh refinement in electrical impedance tomography. *Physiological measurement*, 23(1):121, 2002.

[95] Marc Molinari, SJ Cox, BH Blott, and Geoffrey J Daniell. Adaptive mesh refinement techniques for electrical impedance tomography. *Physiological Measurement*, 22(1):91, 2001.

[96] T Morimoto, Y Kinouchi, T Iritani, S Kimura, Y Konishi, N Mitsuyama, K Komaki, and Y Monden. Measurement of the electrical bio-impedance of breast tumors. *European surgical research*, 22(2):86–92, 1990.

[97] Jennifer L Mueller, David Isaacson, and Jonathan C Newell. A reconstruction algorithm for electrical impedance tomography data collected on rectangular electrode arrays. *Biomedical Engineering, IEEE Transactions on*, 46(11):1379–1386, 1999.

[98] Ethan K Murphy and Jennifer L Mueller. Effect of domain shape modeling and measurement errors on the 2-D D-bar method for EIT. *Medical Imaging, IEEE Transactions on*, 28(10):1576–1584, 2009.

[99] Adrian Nachman and Brian Street. Reconstruction in the calderón problem with partial data. *Communications in Partial Differential Equations*, 35(2):375–390, 2010.

[100] Frank Natterer. *The mathematics of computerized tomography*, volume 32. Siam, 1986.

[101] S Nour, YF Mangnall, JAS Dickson, AG Johnson, and RG Pearse. Applied potential tomography in the measurement of gastric emptying in infants. *Journal of pediatric gastroenterology and nutrition*, 20(1):65–72, 1995.

[102] Tong In Oh, Hun Wi, Do Yub Kim, Pil Joong Yoo, and Eung Je Woo. A fully parallel multi-frequency EIT system with flexible electrode configuration: KHU Mark 2. *Physiological measurement*, 32(7):835, 2011.

[103] Tong In Oh, Eung Je Woo, and David Holder. Multi-frequency EIT system with radially symmetric architecture: KHU Mark 1. *Physiological measurement*, 28(7):S183, 2007.

[104] KS Osterman, TE Kerner, DB Williams, A Hartov, SP Poplack, and KD Paulsen. Multifrequency electrical impedance imaging: preliminary in vivo experience in breast. *Physiological measurement*, 21(1):99, 2000.

[105] Ronal Pethig. Dielectric properties of biological materials: Biophysical and medical applications. *Electrical Insulation, IEEE Transactions on*, (5):453–474, 1984.

[106] G Piperno, EH Frei, and M Moshitzky. Breast cancer screening by impedance measurements. *Frontiers of medical and biological engineering: the international journal of the Japan Society of Medical Electronics and Biological Engineering*, 2(2):111–117, 1989.

[107] Nicholas Polydorides. *Image reconstruction algorithms for soft-field tomography*. PhD thesis, University of Manchester: UMIST, 2002.

[108] Nick Polydorides and William RB Lionheart. A matlab toolkit for three-dimensional electrical impedance tomography: a contribution to the Electrical Impedance and Diffuse Optical Reconstruction Software project. *Measurement Science and Technology*, 13(12):1871, 2002.

[109] Sachin N Prasad, Dana Houserkova, Jan Campbell, et al. Breast imaging using 3D electrical impedence tomography. *Biomedical Papers*, 152(1):151–154, 2008.

[110] A Romsauerova, A McEwan, Lior Horesh, R Yerworth, RH Bayford, and David S Holder. Multi-frequency electrical impedance tomography (EIT) of the adult human head: initial findings in brain tumours, arteriovenous malformations and chronic stroke, development of an analysis method and calibration. *Physiological measurement*, 27(5):S147, 2006.

[111] Grimnes S. Impedance measurement of individual skin surface electrodes. *Med. Biol. Eng. Comput.*, 21:750–755, 1983.

[112] Gary J Saulnier, Ning Liu, Chandana Tamma, Hongjun Xia, Tzu-Jen Kao, JC Newell, and David Isaacson. An electrical impedance spectroscopy system for breast cancer detection. In *Engineering in Medicine and Biology Society, 2007. EMBS 2007. 29th Annual International Conference of the IEEE*, pages 4154–4157. IEEE, 2007.

[113] Joachim Schöberl. NETGEN an advancing front 2D/3D-mesh generator based on abstract rules. *Computing and visualization in science*, 1(1):41–52, 1997.

[114] Herman P Schwan. Electrical properties of body tissues and impedance plethysmography. *Medical Electronics, IRE Transactions on*, pages 32–46, 1955.

[115] Herman P Schwan. Electric characteristics of tissues. *Radiation and Environmental Biophysics*, 1(3):198–208, 1963.

[116] Herman P Schwan and Kenneth R Foster. RF-field interactions with biological systems: electrical properties and biophysical mechanisms. *Proceedings of the IEEE*, 68(1):104–113, 1980.

[117] HP Schwan. Electrical properties of tissues and cell suspensions: mechanisms and models. In *Engineering in Medicine and Biology Society, 1994. Engineering Advances: New Opportunities for Biomedical Engineers. Proceedings of the 16th Annual International Conference of the IEEE*, pages A70–A71. IEEE, 1994.

[118] Erkki Somersalo, Margaret Cheney, and David Isaacson. Existence and uniqueness for electrode models for electric current computed tomography. *SIAM Journal on Applied Mathematics*, 52(4):1023–1040, 1992.

[119] Erkki Somersalo, Margaret Cheney, David Isaacson, and Eli Isaacson. Layer stripping: a direct numerical method for impedance imaging. *Inverse problems*, 7(6):899, 1991.

[120] Nirmal K Soni, Alex Hartov, Christine Kogel, Steven P Poplack, and Keith D Paulsen. Multi-frequency electrical impedance tomography of the breast: new clinical results. *Physiological measurement*, 25(1):301, 2004.

[121] John Sylvester and Gunther Uhlmann. A global uniqueness theorem for an inverse boundary value problem. *Annals of mathematics*, pages 153–169, 1987.

[122] Gerald Sze. *Detection of breast cancer with electrical impedance mammography*. PhD thesis, University of Sussex, 2012.

[123] Albert Tarantola. *Inverse problem theory and methods for model parameter estimation*. siam, 2005.

[124] AT Tidswell, Adam Gibson, RH Bayford, and David S Holder. Electrical impedance tomography of human brain activity with a two-dimensional ring of scalp electrodes. *Physiological measurement*, 22(1):167, 2001.

[125] Andrey Nikolayevich Tikhonov. On the stability of inverse problems. In *Dokl. Akad. Nauk SSSR*, volume 39, pages 195–198, 1943.

[126] Gunther Uhlmann. Electrical impedance tomography and calderón's problem. *Inverse Problems*, 25(12):123011, 2009.

[127] Marko Vauhkonen. Electrical impedance tomography and prior information. 1997.

[128] Marko Vauhkonen, William RB Lionheart, Lasse M Heikkinen, Päivi J Vauhkonen, and Jari P Kaipio. A MATLAB package for the EIDORS project to reconstruct two-dimensional EIT images. *Physiological Measurement*, 22(1):107, 2001.

[129] Marko Vauhkonen, D Vadasz, Pasi A. Karjalainen, Erkki Somersalo, and Jari P. Kaipio. Tikhonov regularization and prior information in electrical impedance tomography. *Medical Imaging, IEEE Transactions on*, 17(2):285–293, 1998.

[130] Päivi J Vauhkonen, Marko Vauhkonen, Tuomo Savolainen, and Jari P Kaipio. Three-dimensional electrical impedance tomography based on the complete electrode model. *Biomedical Engineering, IEEE Transactions on*, 46(9):1150–1160, 1999.

[131] W Wang, B Tunstall, D Chauhan, and M McCormick. The design of De Montfort Mk2 electrical impedance mammography system. In *Engineering in Medicine and Biology Society, 1998. Proceedings of the 20th Annual International Conference of the IEEE*, volume 2, pages 1042–1043. IEEE, 1998.

[132] Hun Wi, Harsh Sohal, Alistair Lee McEwan, Eung Je Woo, and Tong In Oh. Multi-frequency electrical impedance tomography system with automatic self-calibration for long-term monitoring. *Biomedical Circuits and Systems, IEEE Transactions on*, 8(1):119–128, 2014.

[133] Eung Je Woo, Ping Hua, John G Webster, Willis J Tompkins, and Ramón Pallás-Areny. Walsh function current patterns and data synthesis for electrical impedance tomography. *Medical Imaging, IEEE Transactions on*, 11(4):554–559, 1992.

[134] Gang Ye, Kim Hwa Lim, Rhett George, Gary Ybarra, William T Joines, and Qing Huo Liu. A 3D EIT system for breast cancer imaging. In *Biomedical Imaging: Nano to Macro, 2006. 3rd IEEE International Symposium on*, pages 1092–1095. IEEE, 2006.

[135] Gang Ye, Kim Hwa Lim, Rhett T George, Gary A Ybarra, William T Joines, and Qing Huo Liu. 3D EIT for breast cancer imaging: System, measurements, and reconstruction. *Microwave and Optical Technology Letters*, 50(12):3261–3271, 2008.

[136] Rebecca J Yerworth, RH Bayford, B Brown, P Milnes, M Conway, and David S Holder. Electrical impedance tomography spectroscopy (EITS) for human head imaging. *Physiological measurement*, 24(2):477, 2003.

[137] Xiaolin Zhang, Wei Wang, G. Sze, D. Barber, and C. Chatwin. An image reconstruction algorithm for 3D electrical impedance mammography. *Medical Imaging, IEEE Transactions on*, 33(12):2223–2241, Dec 2014.

[138] Michael S Zhdanov. Electromagnetic geophysics: Notes from the past and the road ahead. *Geophysics*, 75(5):75A49–75A66, 2010.

[139] Y Zou and Z Guo. A review of electrical impedance techniques for breast cancer detection. *Medical engineering & physics*, 25(2):79–90, 2003.

List of Abbreviations

BiCG	Bi-Conjugate Gradients
CG	Conjugate Gradients
CT	Computed Tomography
EIDORS	Electrical Impedance and Diffuse Optical Reconstruction Software
EIM	Electrical Impedance Mapping
EIS	Electrical Impedance Spectroscopy
EIT	Electrical Impedance Tomography
ERT	Electrical Resistivity Tomography
FEM	Finite Element Method
MFEIT	Multi-frequency Electrical Impedance Tomography
MRI	Magnetic Resonance Imaging
PCG	Preconditioned Conjugate Gradients
SNR	Signal-to-Noise Ratio
SSRM	Subspace Regularization Method
SVD	Singular Value Decomposition
TSVD	Truncated Singular Value Decomposition
TV	Total Varation (reconstruction)